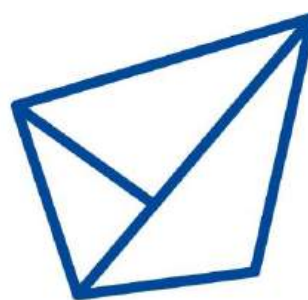


*Report on Eu^{3+} and $\text{Bi}^{3+}/\text{Eu}^{3+}$ -activated
phosphors properties
WP1 (D1.2)*



LEDtech-GROW

*LED TECHNOLOGY BASED ON BISMUTH-SENSITIZED Eu^{3+}
LUMINESCENCE FOR COST-EFFECTIVE INDOOR PLANT
GROWTH*

PROGRAM-PROMIS-2024-2025

Grant Agreement: 10412

Deliverable 1.2
Report on Eu^{3+} and $\text{Bi}^{3+}/\text{Eu}^{3+}$ -activated phosphors properties
Contractual Date Delivery: 03/04/2025

Project Deliverable Information Sheet

LEDtech- GROW Project

Project Ref. No. 10412

Project Title: *LED technology based on bismuth-sensitized Eu^{3+} luminescence for cost-effective indoor plant growth*

Call: Program PROMIS 2023

Starting Date: 03/01/2024

Duration: 24 months

Project Website: <https://ledtechgrow-promis.org/>

Deliverable No.: D1.2

Deliverable Type: Document

Month of delivery: 15

Contractual Delivery Date: 03/04/2025

Actual Delivery Date: 03/04/2025

Principal investigator: Dr. BOJANA MILIĆEVIĆ

Abstract: The report includes a description of the structural, morphological, and optical properties of prepared traditional Eu^{3+} and $\text{Bi}^{3+}/\text{Eu}^{3+}$ -activated fluoride phosphors, as well as a novel generation of Eu^{3+} and $\text{Bi}^{3+}/\text{Eu}^{3+}$ -activated fluoride phosphors. This report is a result of a joint effort between subactivities **1.3** - Structural, morphological, and optical analysis of phosphors and **1.4** - Temperature-dependent photoluminescence, quantum efficiency, and chemical stability of phosphor.

Document Control Sheet

Document

Title: Report on Eu^{3+} and $\text{Bi}^{3+}/\text{Eu}^{3+}$ -activated phosphors properties.docx

Distributed to LEDtech-GROW Participants

Authorship

Written by Aleksandar Ćirić

Contributed by Ljubica Đaćanin Far and Jovana Periša

Approved by Bojana Milićević

Executive Summary

The presented document constitutes Deliverable D1.2 – *Report on Eu^{3+} and $\text{Bi}^{3+}/\text{Eu}^{3+}$ -activated phosphors properties*, the LEDtech-GROW project. It is a public document, delivered in the context of **WP1** - *Design, synthesis, and characterization of plant-grow-targeted phosphors*, **Subactivity 1.3** - *Structural, morphological, and optical analysis of phosphors [month: 6-15]* and **Subactivity 1.4** - *Temperature-dependent photoluminescence, quantum efficiency, and chemical stability of phosphor [month: 6-15]*. This document outlines the detailed properties of prepared Eu^{3+} and $\text{Bi}^{3+}/\text{Eu}^{3+}$ -activated phosphors for sharing and disseminating information related to the LEDtech-GROW project.

Table of Contents

1. Properties of $\text{Sr}_2\text{GdF}_7:\text{Eu}^{3+}$ and $\text{Sr}_2\text{GdF}_7:\text{Bi}^{3+},\text{Eu}^{3+}$	Error! Bookmark not defined.
2. Properties of $\text{Sr}_2\text{LaF}_7:\text{Bi}^{3+},\text{Eu}^{3+}$	13
3. Properties of $\text{SrF}_2:\text{Eu}^{3+}$ and $\text{SrF}_2:\text{Bi}^{3+},\text{Eu}^{3+}$	14
4. Properties of $\text{BaF}_2:\text{Eu}^{3+}$	18
5. Properties of $\text{BaYF}_5:\text{Eu}^{3+}$ and $\text{BaYF}_5:\text{Bi}^{3+},\text{Eu}^{3+}$	19
6. Properties of $\text{BaGdF}_5:\text{Bi}^{3+},\text{Eu}^{3+}$	25
7. Properties of $\text{RbY}_3\text{F}_{10}:\text{Eu}^{3+}$	26
8. Properties of $\text{GdF}_3:\text{Bi}^{3+},\text{Eu}^{3+}$	29
9. Properties of $\text{LuF}_3:\text{Eu}^{3+}$	30
10. Scientific Publications and Peer-Reviewed Journals.....	32

Copyright Notice

Copyright © 2024 LEDtech-GROW project team. All rights reserved. LEDtech-GROW is a project funded by the Science Fund of the Republic of Serbia under grant agreement no. 10412. For more information on the project and contributors please see <https://ledtechgrow-promis.org/>. It is allowed to copy and distribute verbatim copies of this document containing this copyright notice; however, the modification of this document is forbidden.

Disclaimer

Vinča Institute is solely responsible for the content of this publication, and this content does not express the views of the Science Fund of the Republic of Serbia.

Abbreviations and Acronyms

	Explanation
[BYF]	BaYF_5
[BGF]	BaGdF_5
[CCT]	Correlated Color Temperature
[EDTA]	Ethylenediaminetetraacetic acid
[ET]	Energy transfer
[ICDD]	International Centre for Diffraction Data
[LEDtech-GROW]	Acronym of the Project Titled " <i>LED technology based on bismuth-sensitized Eu^{3+} luminescence for cost-effective indoor plant growth</i> "
[Open Access]	Open access publishing (gold or green open access) means that an article is immediately provided in open-access mode on the publisher or journal's website. Some publishers charge Article Processing Charges (APCs) to make articles open.
[PL]	Photoluminescence emission spectra
[P _R]	Phytochrome photoreceptors with absorption peak in the red spectral area
[P _{FR}]	Phytochrome photoreceptors with absorption peak in far-red spectral area
[PXRD]	Powder X-ray diffraction
[QE]	Quantum efficiency
[RYF]	$\text{RbY}_3\text{F}_{10}$
[SEF]	Sr_2EuF_7
[SGF]	Sr_2GdF_7
[TEM]	Transmission electron microscopy
[VinaR]	VinaR, i.e. Vinca Repository is a joint digital repository of all laboratories and departments in Vinča Institute of Nuclear Sciences, University of Belgrade.
[VINS]	"Vinča" Institute of Nuclear Sciences – National Institute of the Republic of Serbia, University of Belgrade
[WP]	Work package

1. Properties of $\text{Sr}_2\text{GdF}_7:\text{Eu}^{3+}$ and $\text{Sr}_2\text{GdF}_7:\text{Bi}^{3+}, \text{Eu}^{3+}$

1.1 Structure, morphology, and diffuse reflectance of Eu^{3+} -doped Sr_2GdF_7 – WP1, sub-activity 1.3

Powder X-ray diffraction (PXRD) patterns of $\text{Sr}_2\text{Gd}_{1-x}\text{Eu}_x\text{F}_7$ ($x = 0, 0.05, 0.10, 0.40, 0.60, 0.80,$ and 1.00) nanophosphors are shown in Figure 1, with Rietveld refinement fits for the two end members, Sr_2GdF_7 (SGF) and Sr_2EuF_7 (SEF), given as Figure 1b-c ($R_{\text{wp}} = 2.72\%$ and 3.43% , respectively). The patterns of Sr_2GdF_7 and Sr_2EuF_7 were fitted using a structural model in the cubic space group $Fm\bar{3}m$ (225), with Sr and Gd ions on Wyckoff site 4a with $m-3m$ symmetry and F ions on Wyckoff site 8c with $-43m$ symmetry. While in the ideal fluorite-type compound of MX_2 stoichiometry, the cations are found in 8-coordinate cubic environments and the anions in 4-coordinate tetrahedral environments, the partial occupancies of both cation and anion sites in Sr_2GdF_7 and Sr_2EuF_7 result in deviations from these ideal coordination geometries and a range of environments is expected to exist for the species present. The obtained unit cell parameters were $5.7484(1)$ Å for SGF and $5.7618(1)$ Å for SEF. All observed reflections were accounted for in the PXRD patterns of all samples, and the absence of extra peaks confirms the phase purity of the materials prepared. Due to the smaller ionic radii of Gd^{3+} ($\text{Gd}_{\text{VIII}}^{3+} = 1.053$ Å) incorporation of larger Eu^{3+} ($\text{Eu}_{\text{VIII}}^{3+} = 1.066$ Å) ions resulted in the shifting of diffraction peaks to lower Bragg angles, consistent with the unit cell parameters obtained for the two end members (see Figure 11d).

Transmission electron microscopy (TEM) images of representative colloidal SGF_40% Eu^{3+} particles, obtained with different magnifications, are shown in Figure 1e-f. Nanoparticles show a similar quasi-spherical shape with the average particle size estimated to be 24 ± 2 nm (see the histogram fitted with a log-normal distribution, based on around 200 particles, Figure 11e inset).

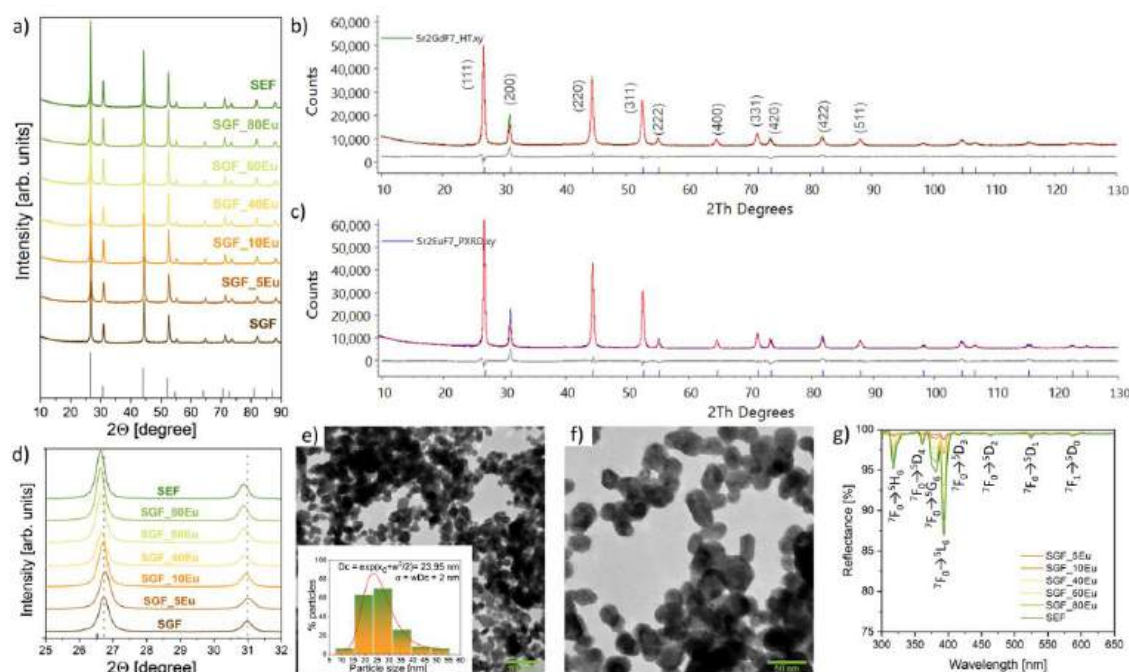


Figure 1. (a) PXRD patterns of $\text{Sr}_2\text{Gd}_{1-x}\text{Eu}_x\text{F}_7$ ($x = 0.05, 0.10, 0.40, 0.60, 0.80,$ and 1.00) nanophosphors; (b, c) Rietveld fits for Sr_2GdF_7 and Sr_2EuF_7 . Green (SGF) and blue (SEF) curves represent the observed pattern, in each case, the red curves are the calculated patterns, and the difference curves are shown in grey, while blue tick marks represent the

positions of the Bragg peaks; (d) Enlarged (111) and (200) diffraction peaks showing a shift toward lower Bragg angles due to the replacement of Gd with Eu ions in the host material; (e, f) TEM images under different magnification with the particle size distribution of representative colloidal SGF:40mol% Eu³⁺ given as Inset in Figure 1e; (g) Room temperature diffuse reflectance spectra for all Sr₂Gd_{1-x}Eu_xF₇ (x = 0.05, 0.10, 0.40, 0.60, 0.80, and 1.00) samples.

Figure 1g shows the room temperature diffuse reflectance spectra of Sr₂Gd_{1-x}Eu_xF₇ (x = 0, 0.05, 0.10, 0.40, 0.60, 0.80, and 1.00) samples in the 300–650 nm wavelength range, which display typical optical features of Eu³⁺ ions. The absorption peaks of Eu³⁺ ions, which are located at 317, 360, 381, 394, 414, 464, 525, and 587 nm correspond to the following electronic transitions: ⁷F₀ → ⁵H₃, ⁷F₀ → ⁵D₄, ⁷F₀ → ⁵G₆, ⁷F₀ → ⁵L₆, ⁷F₀ → ⁵D₃, ⁷F₀ → ⁵D₂, ⁷F₀ → ⁵D₁, and ⁷F₁ → ⁵D₀, respectively, with the highest absorption at around 394 nm.

1.2 Photoluminescent properties of Eu³⁺-doped Sr₂GdF₇ – WP1, sub-activity 1.3

The room temperature photoluminescence excitation spectra of all Sr₂Gd_{1-x}Eu_xF₇ colloids recorded in the 250–330 nm (λ_{em} = 698 nm) and 310–570 nm (λ_{em} = 593 nm) ranges are given in Figure a-b, showing lines that correspond to transitions within the 4f⁶ configuration of Eu³⁺ and 4f⁷ configuration of Gd³⁺. Excitations centered around 273 and 311 nm correspond to Gd³⁺ absorption. The intensity of Gd³⁺ peaks is the largest for the Sr₂Gd_{0.9}Eu_{0.1}F₇ composition (90 mol% of Gd³⁺ and 10 mol% of Eu³⁺), indicating the optimal Eu/Gd ratio for energy transfer from Gd³⁺ to Eu³⁺.

Photoluminescence emission spectra of all Sr₂Gd_{1-x}Eu_xF₇ colloids recorded at room temperature are given in Figure c (λ_{ex} = 273 nm) and Figure d (λ_{ex} = 394 nm). Emission centered at 311 nm, presented in Figure c, corresponds to the ⁶P₁ → ⁸S_{7/2} transition of Gd³⁺, while those at longer wavelengths correspond to 4f–4f transitions of Eu³⁺ (Figure d) placed at ~592 nm (⁵D₀ → ⁷F₁), ~613 nm (⁵D₀ → ⁷F₂), ~650 nm (⁵D₀ → ⁷F₃), and ~700 nm (⁵D₀ → ⁷F₄). If the excitation is in the Gd³⁺ ion, either Gd³⁺ radiates with 310 nm emission or transfers energy to the Eu³⁺. Then the Eu³⁺ ion de-excites to the lower excited levels from which it radiatively de-excites to the ground multiplet. Alternatively, the Eu³⁺ may absorb UV photons directly, most efficiently at 394 nm, and undergo the same de-excitation pathway as with the ET from the Gd³⁺ ion. These mechanisms are depicted in Figure 2e. Emission peaks from ⁵D₁, ⁵D₂, and ⁵D₃ levels (Figure d inset) are the most intense with 10 mol% of Eu³⁺ because of earlier concentration quenching of energetically higher Eu³⁺ levels.

The ⁵D₀ → ⁷F₁ is a magnetic-dipole transition that does not depend on the local environment. However, the ⁵D₀ → ⁷F₂ electric-dipole transition is a hypersensitive one and highly dependent on changes in the local environment around the Eu³⁺ ions. Theoretically, when the Eu³⁺ ions occupy centrosymmetric sites, the emission spectrum shows a more intense ⁵D₀ → ⁷F₁ transition than the ⁵D₀ → ⁷F₂ one. This agrees with our experimental observations. In addition, the ratio of the integrated intensity of the ⁵D₀ → ⁷F₂ and ⁵D₀ → ⁷F₁ transitions, known as the asymmetry ratio, can be considered indicative of the reduction of symmetry of the coordination environment around the Eu³⁺ ion and is given by eq.:

$$R = \frac{I(^5D_0 \rightarrow ^7F_2)}{I(^5D_0 \rightarrow ^7F_1)}. \quad (1)$$

The asymmetry ratio values obtained from the emission spectra do not vary significantly as a function of Eu³⁺ concentration, as shown in Figure 2f. Therefore, one may conclude that the degree of distortion of the local symmetry around Eu³⁺ is similar in the samples in the series produced. This is consistent with the samples being isostructural, as shown by PXRD and Rietveld analysis.

Emission in the deep-red spectral region around 700 nm, which corresponds to the ⁵D₀ → ⁷F₄

transition, exhibits high intensity, even higher than emission from ${}^5D_0 \rightarrow {}^7F_1$ and ${}^5D_0 \rightarrow {}^7F_2$ transitions. This is not common for Eu³⁺ and it was previously reported for several fluoride hosts where the structural distortion from the octahedral symmetry to the non-centrosymmetric D_{4d} occurs, as the odd-rank components of the static forced electric dipole and ligand polarizability-dependent dynamic coupling mechanisms are high, especially in the highly polarizable chemical environment. This observation in our spectra is consistent with a range of Eu³⁺ environments present and the breaking of the centrosymmetric $m\text{-}3m$ symmetry of the average long-range crystallographic model at a local level, due to the partial site occupancies. Figure g shows that photoluminescent intensity continually increases as the Eu³⁺ content increases from 5 mol% to 80 mol%, without concentration quenching. The Eu³⁺ deep-red emission (${}^5D_0 \rightarrow {}^7F_4$) in SGF:Eu phosphors have a full width at a half-maximum of around 10 nm and fits the absorption band of phytochrome photoreceptors, P_{FR}. Furthermore, the Eu³⁺ red emission bands (${}^5D_0 \rightarrow {}^7F_1$ and ${}^5D_0 \rightarrow {}^7F_2$) matched the red-adsorbing phytochrome photoreceptors, P_R, indicating that SGF:Eu may be an effective nanophosphor for horticulture LED applications. To evaluate real application potential, the absolute photoluminescent quantum efficiency was measured at room temperature with an integrating sphere, and the results are shown in Figure g. The efficiency increases with Eu³⁺-dopant concentration starting from 7% for the 5 mol% doped sample and reaching 60% for the 80% doped sample.

Figure h displays the normalized photoluminescent lifetime decay curves of the Sr₂Gd_{1-x}Eu_xF₇ ($x = 0.05, 0.10, 0.40, 0.60, 0.80, \text{ and } 1.00$) colloids recorded at room temperature. To obtain the value of the lifetime (τ), acquired data were fitted to a simple single exponential function:

$$I(t) = I_0 e^{-\frac{t}{\tau}}, \quad (2)$$

where $I(t)$ represents the emission intensity at time t , I_0 represents the initial emission intensity ($I_0 = 1$ in normalized curves in Figure 2h), and τ represents the emission decay constant (excited state lifetime). As the Eu³⁺ concentration increased, the 5D_0 -level lifetimes gradually decreased from 12.0 to 6.9 ms. The shortening of the lifetime with increasing concentration indicates the activation of concentration-quenching mechanisms. These quenching mechanisms compete with the increase in emission intensity due to an increase in the number of optically active centers when Eu³⁺ concentration is increased, resulting in an intensity net rise with concentrations up to 80% of Eu³⁺ content.

Chromaticity coordinates (x, y) on the CIE chromaticity diagram, a two-dimensional color space that describes all the colors observed by the human eye, can be used to quantify apparent color. We derived the CIE chromaticity coordinates from the photoluminescent spectra to evaluate the color of the synthesized samples, as shown in Figure 2i and Table 1. For all the samples, CIE coordinates are almost identical for the highly doped samples ($x = 0.62, y = 0.38; \lambda_{\text{dom}} = 598 \text{ nm}; \text{color purity} = 99.1\%$) and placed in the orange-red portion of the diagram, confirming that there is no significant change in the local symmetry around Eu³⁺ across the series and consequently in the emission spectra. Inset in Figure 2i shows the translucent white color of colloids under daylight and the red appearance of colloids under UV light.

Table 1 Chromaticity coordinates (x, y) of SGF:Eu

	SGF_5Eu	SGF_10Eu	SGF_40Eu	SGF_60Eu	SGF_80Eu	SEF
CIE (x, y) coordinates	(0.565,0.398)	(0.586,0.396)	(0.611,0.384)	(0.615,0.381)	(0.616,0.381)	(0.614,0.383)

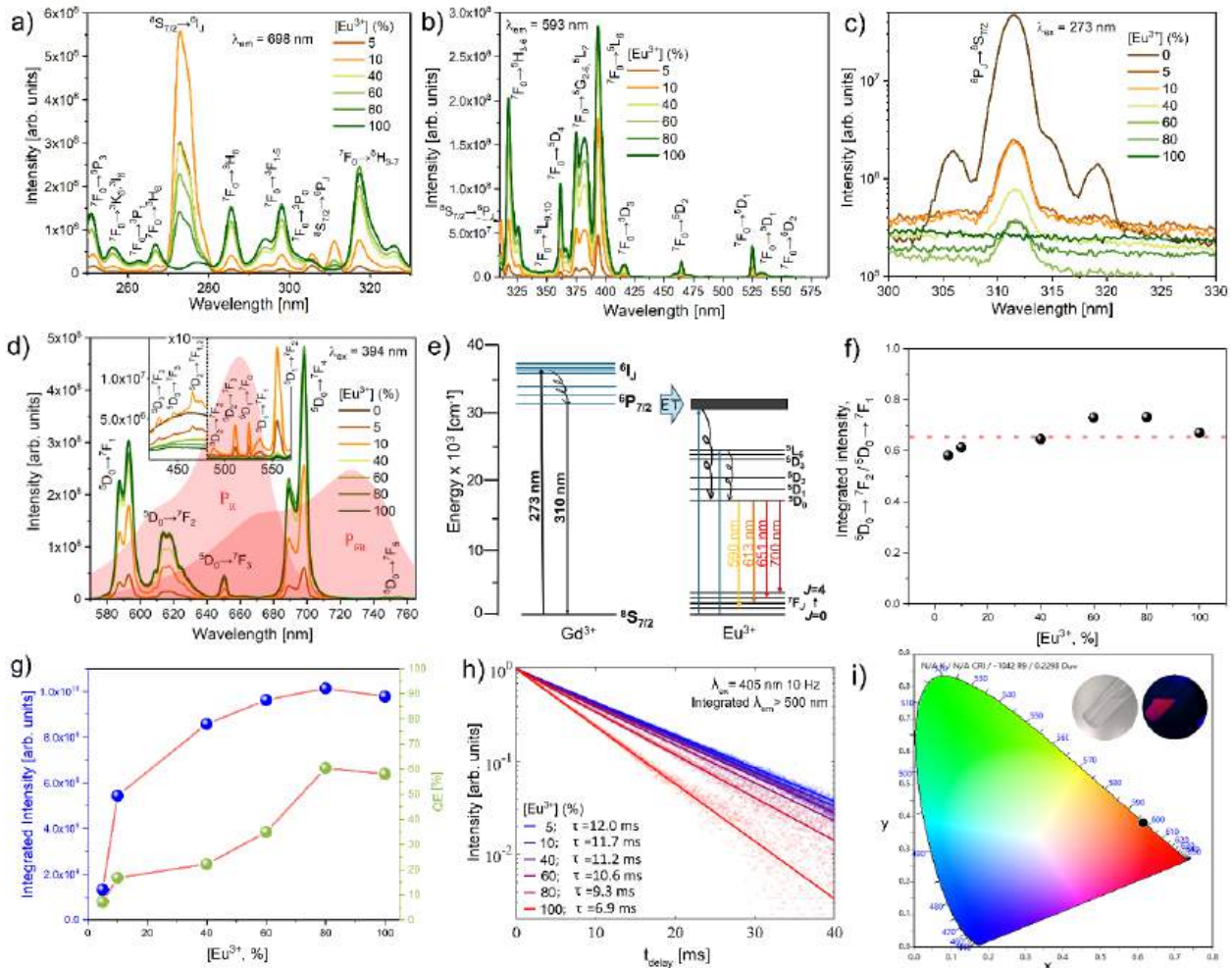


Figure 2. Room temperature photoluminescence of $\text{Sr}_2\text{Gd}_{1-x}\text{Eu}_x\text{F}_7$ ($x = 0.05, 0.10, 0.40, 0.60, 0.80,$ and 1.00) colloids: a) excitation spectra under $\lambda_{em} = 698$ nm; b) excitation spectra under $\lambda_{em} = 593$ nm; c) emission spectra under $\lambda_{ex} = 273$ nm; d) emission spectra under $\lambda_{ex} = 394$ nm (red pattern is the absorption spectra of P_R and P_{FR} photoreceptors); e) energy level diagram and energy transfer mechanism of Gd^{3+} and Eu^{3+} in SGF; f) asymmetry ratio as a function of Eu ions concentration; g) integrated emission intensity as a function of Eu ions concentration (blue dots) and quantum efficiency as a function of Eu ions concentration (green dots); h) lifetime decay curves as a function of Eu ions concentration; and i) CIE diagram with calculated coordinates of SGF_80Eu (Inset: appearance of colloid under daylight and near UV light).

1.3 Temperature-dependent photoluminescence measurements of Eu^{3+} -doped SGF – WP1, sub-activity 1.4

To determine the temperature stability, temperature-dependent photoluminescence measurements in steady-state and time domains were recorded in the 25–200 °C temperature range on dried samples in powder form. Figure 3a shows the white color of powders under daylight and the red appearance under UV light, which becomes more intense as Eu^{3+} concentration increases. Figure 3b shows the lifetime, while Figure 3c shows the emission intensity as a function of temperature for two representative samples, SGF_5Eu (with the lowest Eu^{3+} content in the series) and the SGF_80Eu sample, with the highest emission intensity. For both samples, lifetime values show high-temperature stability in the temperature range relevant for LEDs, while emission intensity shows a slight decrease in the same range. It is important to note that, depending on the manufacturer, 100°C is usually considered the

maximal operating temperature of LEDs, while temperature stability up to 150°C is frequently given in the literature. For SGF_80Eu, the sample with the highest emission intensity, the lifetime, and the emission intensity at 100°C remain at 95% and 83% of their initial values at room temperature, respectively. It is generally acknowledged that Eu³⁺'s 4*f* electrons are effectively shielded, and the primary de-excitation pathways of the ⁵D₀ level occur through cross-over with the charge transfer band or multiphonon relaxation. In fluoride matrices, the charge transfer bands are energetically far from the ⁵D₀ level, and these matrices are characterized by low phonon energies, resulting in a lower probability of temperature-induced de-excitation in SGF:Eu³⁺. However, a marked decline in stability is observed for SGF_80Eu beyond 100°C, in contrast to the consistently stable SGF_5 across all temperatures. This suggests that cross-relaxation effects become more prominent with increasing temperature at higher Eu³⁺ concentrations. In addition to our findings, Table 2 includes previously reported excitation and emission wavelength, quantum efficiency (QE) values, and temperature stability for far-red-emitting phosphors produced for indoor plant growth LEDs. Findings shown in Table 2 are mainly based on Mn⁴⁺-doped phosphors, while the literature reports on the Eu³⁺-activated oxide phosphors as prospective candidates for horticulture LEDs are scarce.

Finally, we mixed the powder sample of the highest emission intensity, SGF_80Eu, with a ceramic binder and placed it on top of a 365 nm near-UV LED chip to demonstrate the application potential of these materials in LEDs. Photographs of the fabricated LED device, presented in Figure 3d, display a red light when the power supply is on. In addition, Figure 3e shows the PL spectrum of the fabricated LED device with CIE coordinates (0.5759, 0.3893) and low correlated color temperature (CCT = 1534 K).

Table 2. QE values and temperature stability for some previously reported far-red phosphors

Far-red-emitting phosphors	λ_{ex} (nm), λ_{em} (nm)	QE (%)	Thermal stability (I _{373K} /I _{303K})	Thermal stability (I _{423K} /I _{303K})
SGF_80Eu	394, 698	60.4	83%	66%
Li ₂ MgZrO ₄ :Mn ⁴⁺	335, 675	32.3	75%	58%
Ca ₂ LuSbO ₆ :Mn ⁴⁺	345, 683	39.1	66%	48%
La ₂ ZnTiO ₆ :Mn ⁴⁺	342, 708	-	81%	64%
CaYAlO ₄ : Mn ⁴⁺	370, 710	26	50%	70%
NaLaMgWO ₆ :Mn ⁴⁺	342, 700	60	-	57%
Ca ₉ MY _{0.667} (PO ₄) ₇ :Eu ³⁺ (M = Li, Na)	394, 700	-	-	-
Lu ₂ GeO ₅ :Bi ³⁺ ,Eu ³⁺	313,710	43	70%	51%

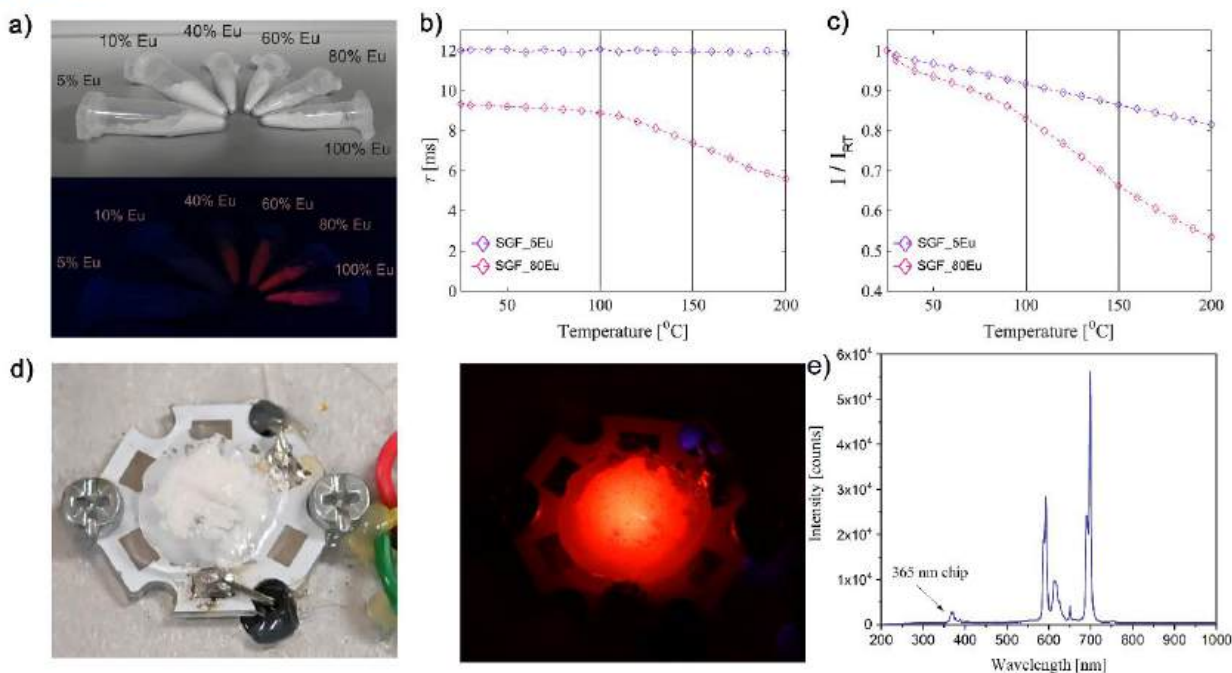


Figure 3. a) Appearance of nanophosphors under daylight and near UV light. Temperature-dependence of b) lifetime and c) emission intensity for the whole set of nanophosphors. d) A fabricated LED device comprising a semiconductor chip and SGF_80Eu nanophosphors displays a red light when the electrical power supply is on. e) PL spectrum of the fabricated LED.

1.4 Structural and optical properties of Bi^{3+} -doped $\text{Sr}_2\text{Gd}_{0.2}\text{Eu}_{0.8}\text{F}_7$ nanoparticles – WP1, sub-activity 1.3

Powder X-ray diffraction patterns of $\text{Sr}_2\text{Gd}_{0.2}\text{Eu}_{0.8}\text{F}_7:x\text{Bi}^{3+}$ ($x = 0.25, 1, 5, \text{ and } 10$ mol%) nanophosphors are shown in Figure 14. The patterns of $\text{Sr}_2\text{Gd}_{0.2}\text{Eu}_{0.8}\text{F}_7:x\text{Bi}^{3+}$ are in accordance with the cubic space group $Fm\bar{3}m$ (225). All observed reflections were accounted for in the PXRD patterns of all samples, and the absence of extra peaks confirms the phase purity of the materials prepared. Due to the smaller ionic radii of Gd^{3+} ($\text{Gd}_{\text{VI}}^{3+} = 1.053 \text{ \AA}$) incorporation of larger Eu^{3+} ($\text{Eu}_{\text{VII}}^{3+} = 1.066 \text{ \AA}$) ions resulted in the shifting of diffraction peaks to lower Bragg angles.

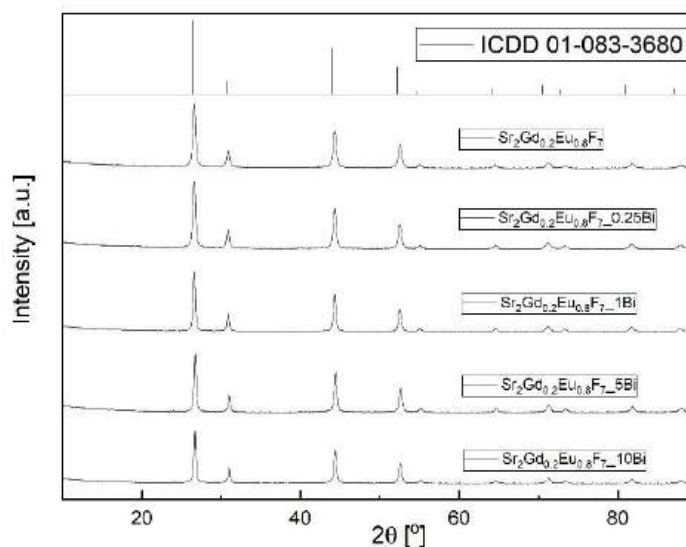


Figure 4. PXRD patterns of $\text{Sr}_2\text{Gd}_{0.2}\text{Eu}_{0.8}\text{F}_7:x\text{Bi}^{3+}$ ($x = 0.25, 1, 5, \text{ and } 10$ mol%) nanophosphors.

The room temperature photoluminescence emission spectra of all of Bi³⁺-co-doped Sr₂Gd_{0.2}Eu_{0.8}F₇ powders recorded in the 420–750 nm ($\lambda_{exc} = 391$ nm) are given in Figure 5, showing lines that correspond to transitions within the 4f⁶ configuration of Eu³⁺. Emissions correspond to 4f–4f transitions of Eu³⁺ placed at ~592 nm (⁵D₀ → ⁷F₁), ~613 nm (⁵D₀ → ⁷F₂), ~650 nm (⁵D₀ → ⁷F₃), and ~700 nm (⁵D₀ → ⁷F₄). Europium ions' emission intensity monotonically increases in the co-doped samples up to 1 mol% of Bi³⁺, while the further addition of Bi³⁺ decreases the emission intensity. The similar asymmetry ratio values and CIE coordinates indicate that there is no significant change in the local symmetry around Eu³⁺ ions or the emission color across the series. This confirms that Eu³⁺ resides in the same crystalline environment in samples. CIE coordinates and correlated color temperature values are presented in Table 3. Energy transfer between bismuth (Bi³⁺) and europium (Eu³⁺) ions in inorganic materials involves the absorption of energy by Bi³⁺ ions, which are excited from their ground state to higher energy levels. This energy is then transferred to Eu³⁺ ions, promoting them from their ground state to excited states. The efficiency of this transfer depends on several factors, including the distance between the ions, the overlap between the emission spectrum of Bi³⁺ and the absorption spectrum of Eu³⁺, and the properties of the host material. This work is still ongoing.

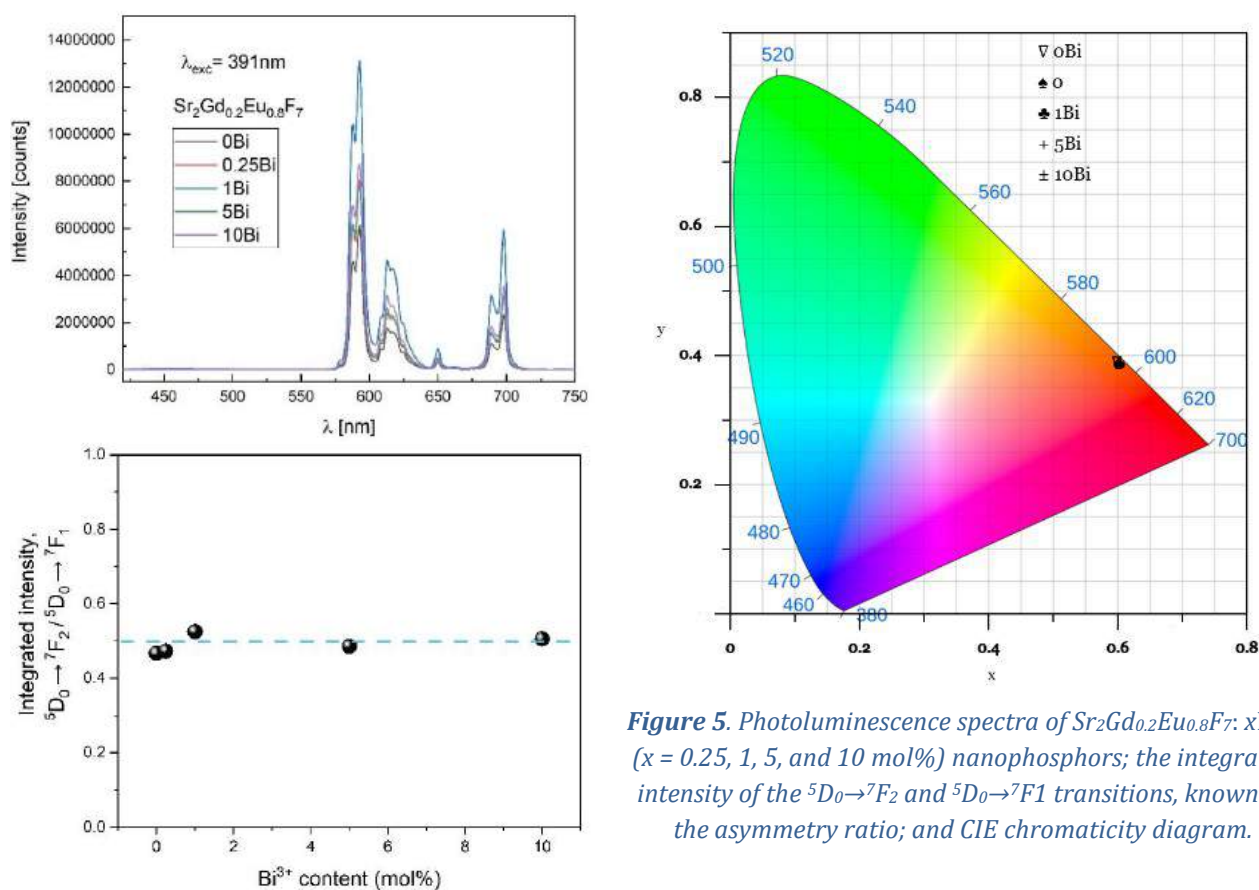


Figure 5. Photoluminescence spectra of Sr₂Gd_{0.2}Eu_{0.8}F₇: xBi³⁺ ($x = 0.25, 1, 5,$ and 10 mol%) nanophosphors; the integrated intensity of the ⁵D₀ → ⁷F₂ and ⁵D₀ → ⁷F₁ transitions, known as the asymmetry ratio; and CIE chromaticity diagram.

Table 3. Chromaticity coordinates (x,y) of Sr₂Gd_{0.2}Eu_{0.8}F₇: xBi³⁺ ($x = 0.25, 1, 5,$ and 10 mol%) nanophosphors.

	Sr ₂ Gd _{0.2} Eu _{0.8} F ₇ (SGEF)	SGEF_0.25Eu	SGEF_1Eu	SGEF_5Eu	SGEF_10Eu
CIE (x, y) coordinates	(0.598,0.388)	(0.601,0.389)	(0.601,0.387)	(0.600,0.389)	(0.602,0.389)
CCT	1727.5	1729.6	1737.0	1730.8	1734.1

2. Properties of $\text{Sr}_2\text{LaF}_7:\text{Bi}^{3+},\text{Eu}^{3+}$

2.1 Structural and optical properties of Bi^{3+} -doped Sr_2LaF_7 (5 mol% Bi^{3+}) – WP1, sub-activity 1.3

Powder X-ray diffraction patterns of $\text{Sr}_2\text{LaF}_7:10\text{mol}\% \text{Eu}^{3+}$ and $\text{Sr}_2\text{LaF}_7:5\text{mol}\% \text{Bi}^{3+}$ nanophosphors are shown in Figure 16. The patterns of $\text{Sr}_2\text{LaF}_7:10\text{mol}\% \text{Eu}^{3+}$ and $\text{Sr}_2\text{LaF}_7:5\text{mol}\% \text{Bi}^{3+}$ match well with the International Centre for Diffraction Data (ICDD) Card No. 00-053-0774, with the cubic space group $Fm\bar{3}m$ (225). Figure 6-down shows lines that correspond to transitions within the $4f^6$ configuration of Eu^{3+} . Emissions below 450 nm correspond to the host material and to the $4f-4f$ transitions of Eu^{3+} placed at $\sim 592 \text{ nm}$ ($^5\text{D}_0 \rightarrow ^7\text{F}_1$), $\sim 613 \text{ nm}$ ($^5\text{D}_0 \rightarrow ^7\text{F}_2$), and $\sim 700 \text{ nm}$ ($^5\text{D}_0 \rightarrow ^7\text{F}_4$). The europium emission intensity monotonically decreases in the co-doped samples up to 10 mol% of Bi^{3+} . We may conclude that energy transfer from Bi^{3+} to Eu^{3+} is not observed in the $\text{Sr}_2\text{La}_{0.9}\text{Eu}_{0.1}\text{F}_7$ nanophosphor.

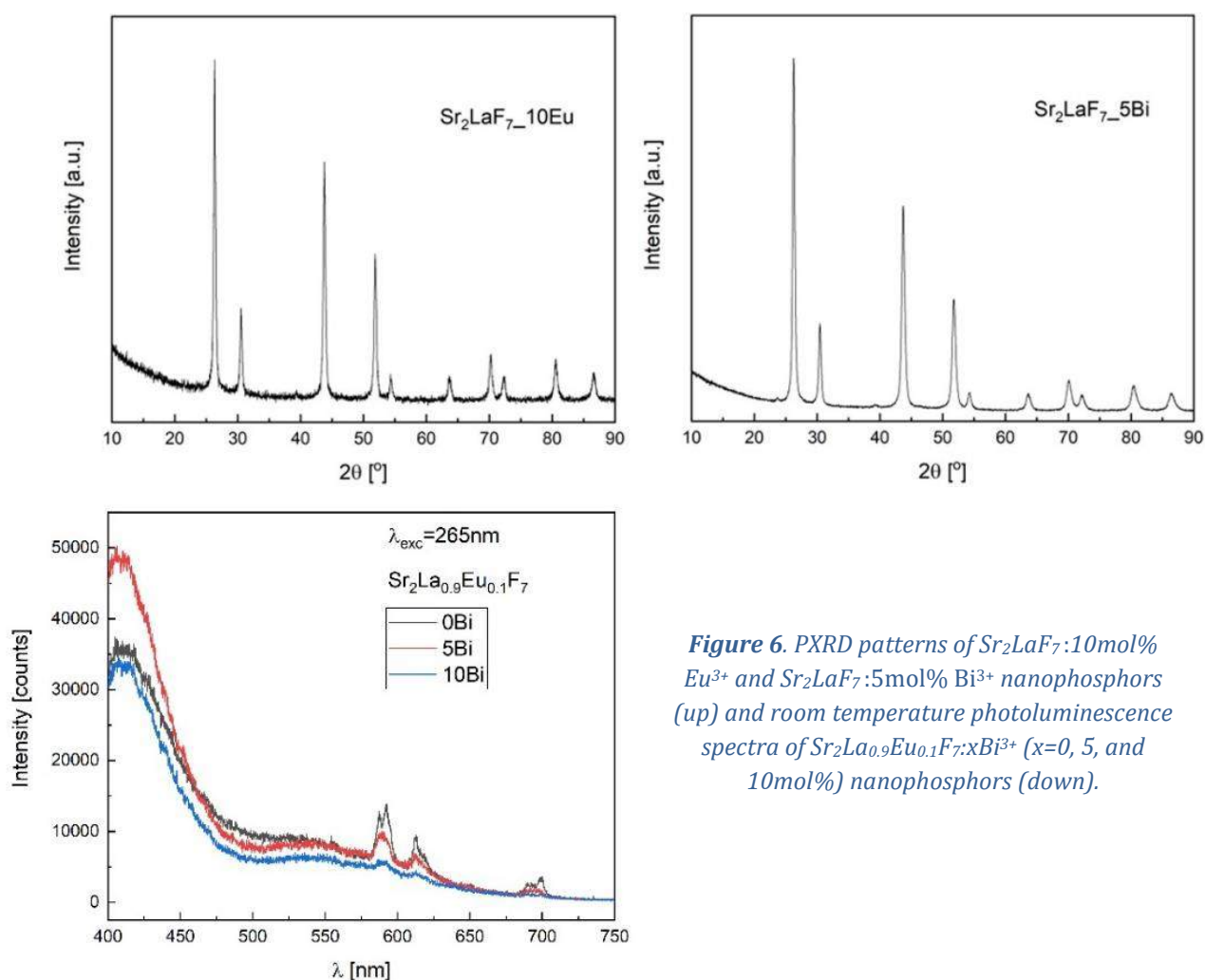


Figure 6. XRD patterns of $\text{Sr}_2\text{LaF}_7:10\text{mol}\% \text{Eu}^{3+}$ and $\text{Sr}_2\text{LaF}_7:5\text{mol}\% \text{Bi}^{3+}$ nanophosphors (up) and room temperature photoluminescence spectra of $\text{Sr}_2\text{La}_{0.9}\text{Eu}_{0.1}\text{F}_7:x\text{Bi}^{3+}$ ($x=0, 5,$ and $10\text{mol}\%$) nanophosphors (down).

3. Properties of $\text{SrF}_2:\text{Eu}^{3+}$ and $\text{SrF}_2:\text{Bi}^{3+},\text{Eu}^{3+}$

3.1 Structure and morphology of Eu^{3+} -doped SrF_2 and $\text{Bi}^{3+}, \text{Eu}^{3+}$ -doped SrF_2 nanoparticles – WP1, sub-activity 1.3

Figures 7a and 7b show the X-ray pattern of $\text{SrF}_2:x\text{Eu}$ ($x= 1, 5, 10, 15, 20$ mol%) and $\text{SrF}_2: 10\text{Eu}y\text{Bi}$ ($y= 5, 10, 15, 20, 30, 40$ mol%) presented with the International Centre for Diffraction Data (ICDD) Card No. 01-086-2418. The X-ray diffraction examination of the synthesized samples proved a single-phase cubic structure with $Fm-3m$ (225) space group (including the $\text{SrF}_2:20\text{Bi}$ sample, Figure 8a). Traces of contamination or other phase peaks were not observed in either set of samples, indicating that dopant $\text{Eu}^{3+}/\text{Bi}^{3+}$ ions were embedded into the SrF_2 lattice. On the contrary, in the case of $\text{SrF}_2:10\text{Eu}50\text{Bi}$ sample, additional peaks originate from a different phase, suggesting the upper limit of dopant ions concentration in the made material has been reached (Figure 8b).

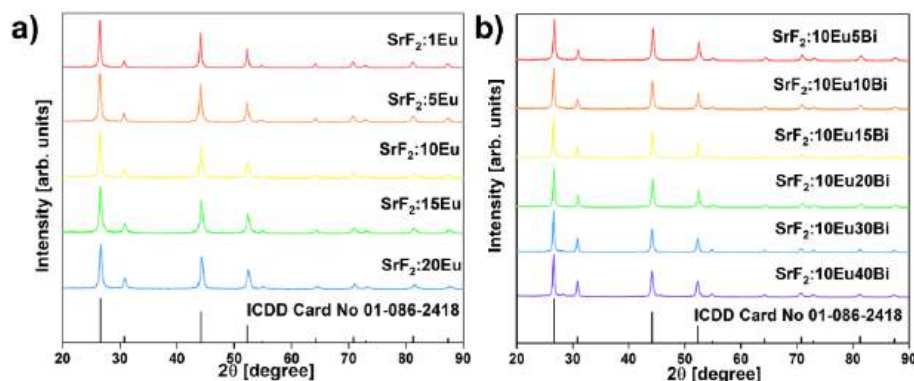


Figure 7. XRD patterns of a) $\text{SrF}_2:x\text{Eu}$ ($x= 1, 5, 10, 15, 20$ mol%) and $\text{SrF}_2: 10\text{Eu},y\text{Bi}$ ($y= 5, 10, 15, 20, 30, 40$ mol%) samples presented with the ICDD card No. 01-086-2418.

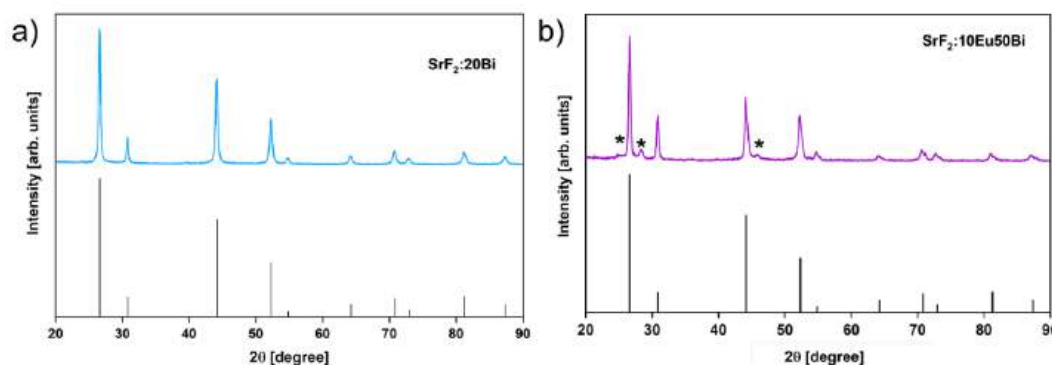


Figure 8. PXRD patterns of a) $\text{SrF}_2:20\text{Bi}$, and b) $\text{SrF}_2:10\text{Eu}50\text{Bi}$ samples. The diffraction peaks are indexed according to the ICDD card No. 01-086-2418.

Additionally, the mean crystallite size and structural parameters are presented in Table 4 (parameters for $\text{SrF}_2:x\text{Eu}$ ($x= 1, 5, 10, 15, 20$ mol%), $\text{SrF}_2:10\text{Eu}y\text{Bi}$ ($y= 5, 10, 15, 20, 30, 40$ mol%), and $\text{SrF}_2:20\text{Bi}$ sample). The average crystallite size (CS) was calculated to be in the nanometer domain ($\sim 14\text{--}25$ nm) for all the samples.

Table 4. Selected structural parameters of the $\text{SrF}_2:\text{xEu}$ ($\text{x} = 1, 5, 10, 15, 20$ mol%), $\text{SrF}_2:10\text{Eu}\text{yBi}$ ($\text{y} = 5, 10, 15, 20, 30, 40$ mol%) and $\text{SrF}_2:20\text{Bi}$ nanopowders.

ICDD card 01-086-2418	a=b=c (Å)	CS (Å)	Strain	GOF	Rwp (%)	Rp (%)	Re (%)
SrF₂:1Eu	5.7970(2)	183.5(11)	0.14(6)	1.0426	7.65	5.77	7.34
SrF₂:5Eu	5.7979(3)	131.2 (11)	0.24(9)	1.0247	7.38	5.77	7.20
SrF₂:10Eu	5.79128(14)	150.2(5)	0.15(3)	1.0261	7.42	5.74	7.23
SrF₂:15Eu	5.7973(5)	117.9 (10)	0.19(9)	1.0567	7.38	5.78	6.98
SrF₂:20Eu	5.7838(5)	123.7 (13)	0.14(3)	1.0936	7.50	5.98	6.86
SrF₂:10Eu5Bi	5.7907(4)	149.0 (18)	0.23(11)	1.1974	8.73	6.79	7.29
SrF₂:10Eu10Bi	5.7914(3)	188(2)	0.06(10)	1.1738	8.64	6.59	7.36
SrF₂:10Eu15Bi	5.7942(4)	209(2)	0.08(7)	1.4142	10.68	7.96	7.55
SrF₂:10Eu20Bi	5.7918(5)	178(3)	0.123(5)	1.4067	10.86	8.10	7.72
SrF₂:10Eu30Bi	5.8023(5)	250(18)	0.220(9)	1.7336	12.84	9.49	7.40
SrF₂:10Eu40Bi	5.8080(13)	201(5)	0.23(8)	1.6523	12.63	9.14	7.87
SrF₂: 20Bi	5.8011(3)	250.5(16)	0.241(5)	1.1840	8.75	6.63	7.39

* Rwp—the weighted profile factor; ** Rp—the profile factor; *** Re—the expected weighted profile factor; GOF—the goodness of fit.

A transmission electron microscopy (TEM) image of the representative $\text{SrF}_2:10\text{Eu}20\text{Bi}$ sample is shown in Figure 9a. Nanoparticles exhibit a pseudo-spherical shape with the average particle size estimated to be 14.2 ± 0.3 nm (see the histogram fitted with a Gaussian distribution, based on around 60 particles, using the largest axis of the grain, Figure 9b). The calculated average particle size roughly equals the crystallite size obtained using X-ray diffraction.

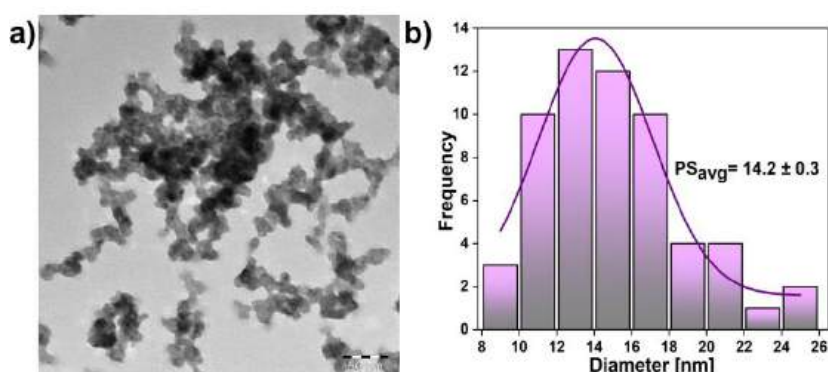


Figure 9. a) TEM images of the representative $\text{SrF}_2:10\text{Eu}20\text{Bi}$ sample, b) particle size distribution histogram.

3.2 Photoluminescence properties of Eu^{3+} -doped SrF_2 and Bi^{3+} , Eu^{3+} -doped SrF_2 nanoparticles – WP1, sub-activity 1.3

The photoluminescence (PL) emission spectra of Eu^{3+} - doped set of samples: $\text{SrF}_2:1\text{Eu}$, $\text{SrF}_2:5\text{Eu}$, $\text{SrF}_2:10\text{Eu}$, $\text{SrF}_2:15\text{Eu}$, and $\text{SrF}_2:20\text{Eu}$ recorded at room temperature are displayed in Figure 10a ($\lambda_{\text{exc}} = 405$ nm). All emissions correspond to $4f-4f$ transitions of Eu^{3+} located at ~ 593 nm ($^5\text{D}_0 \rightarrow ^7\text{F}_1$), ~ 614 nm ($^5\text{D}_0 \rightarrow ^7\text{F}_2$), ~ 651 nm ($^5\text{D}_0 \rightarrow ^7\text{F}_3$), and ~ 700 nm ($^5\text{D}_0 \rightarrow ^7\text{F}_4$). From the obtained emission spectra and integrated PL intensity (Figure 10b) it is evident that the sample $\text{SrF}_2:10\text{Eu}$ shows the highest emission intensity, and for this reason, it has been chosen.

Figure 10c shows the diffuse reflectance spectra of Bi^{3+} co-doped $\text{SrF}_2:10\text{Eu}$ (Bi^{3+} mol% = 5, 10, 15, 20, 30, and 40) samples in the 220–500 nm wavelength range. The spectra show the absorption band at 394 nm corresponding to the Eu^{3+} transition from the ground state $^7\text{F}_0$ to the upper level $^5\text{L}_6$. In addition, it is

observed that the UV band edge redshifts with an increase of Bi^{3+} content, indicating a strong absorption of Bi^{3+} , which lies in the UV region.

Figure 10d shows PL emission spectra of Bi^{3+} -co-doped samples in the 550–725 nm spectral region recorded at room temperature under 265 nm excitation. Europium ions' emission intensity monotonically increases in the co-doped samples up to 20 mol% of Bi^{3+} , while the further addition of Bi^{3+} decreases the emission intensity. The integrated emission intensity in the 550 – 725 nm wavelength range shows that the sample with the highest emission intensity- $\text{SrF}_2:10\text{Eu}20\text{Bi}$ has twice as bright PL compared to the Bi-free $\text{SrF}_2:10\text{Eu}$ phosphor (Figure 10e). Energy transfer (ET) between bismuth (Bi^{3+}) and europium (Eu^{3+}) ions in inorganic hosts involves Bi^{3+} ions absorbing energy and transitioning from their ground state to excited states, followed by energy transfer to Eu^{3+} ions, exciting them from their ground to higher states (Figure 10f). The efficiency of this process depends on factors such as the distance between ions, the spectral overlap between Bi^{3+} emission and Eu^{3+} absorption, and the properties of the host material. When excited, Eu^{3+} electrons radiatively return to the ground state, and emit light at characteristic wavelengths, making this mechanism valuable for applications like LED displays, sensors, and solid-state lasers, and grasping these interactions enables tailoring of optical properties in materials development.

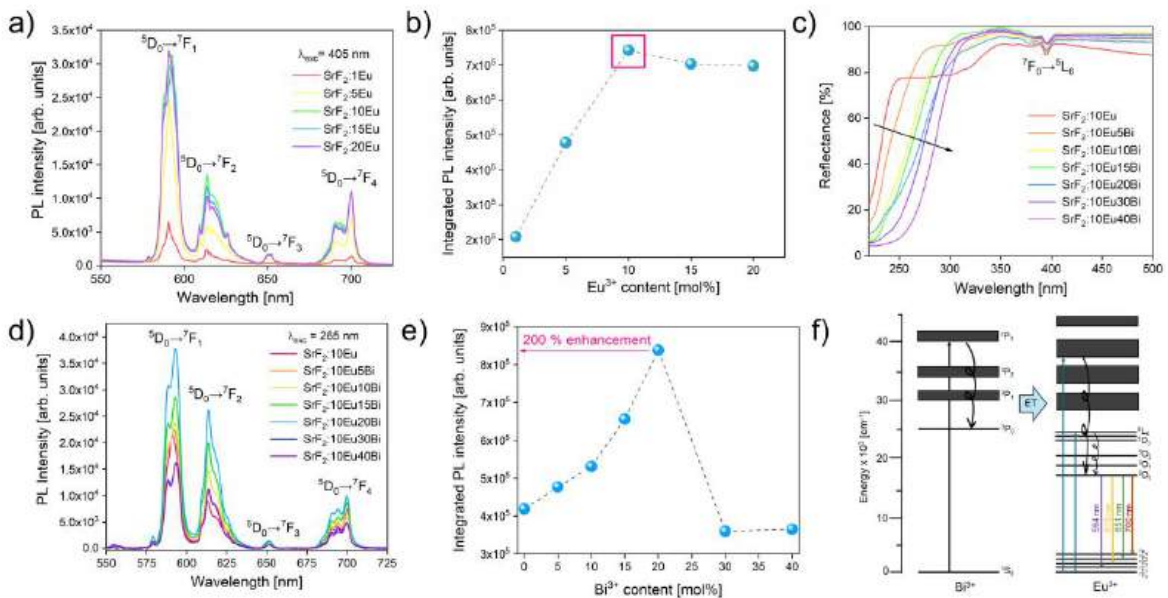


Figure 10. a) Room temperature PL emission spectra under $\lambda_{exc} = 405$ nm of samples doped with only Eu^{3+} ions, b) Integrated intensity of PL spectra presented in a), c) Diffuse reflectance spectra of samples doped with 10 mol% of Eu^{3+} ions and co-doped with Bi^{3+} ions, d) Room temperature PL emission spectra under $\lambda_{exc} = 265$ nm of co-doped samples, e) Integrated intensity of PL spectra presented in d), and f) schematic representation of the possible ET between Bi^{3+} and Eu^{3+} ions.

Figure 11a shows the room temperature PL emission spectra ($\lambda_{exc} = 265$ nm) of $\text{SrF}_2:20\text{Bi}$, $\text{SrF}_2:10\text{Eu}$, and $\text{SrF}_2:10\text{Eu}20\text{Bi}$ samples in the 380–725 nm spectral region, showing both blue and red-light components in different ratios. Emission spectra of $\text{SrF}_2:10\text{Eu}_y\text{Bi}$ ($y = 5, 10, 15, 30,$ and 40 mol%) samples in the 380–725 nm spectral region are presented in Figure 12. Since the intense blue emission is present in both single-doped samples, it can be concluded that it originates from the host material. On account of the energy transfer from Bi^{3+} to Eu^{3+} , it is feasible to attain modifiable emission from blue to red in the $\text{SrF}_2:10\text{Eu}$, Bi co-doped samples system by modulating Bi^{3+} content (5, 10, 15, 20, 30, and 40 mol%). Figure 11b shows the CIE chromaticity diagram for $\text{SrF}_2:20\text{Bi}$, $\text{SrF}_2:10\text{Eu}$, and $\text{SrF}_2:10\text{Eu}_y\text{Bi}$ samples ($y = 5, 10, 15, 20, 30,$ and 40 mol%). The CIE chromaticity coordinates move from blue for the $\text{SrF}_2:20\text{Bi}$

sample, to pinkish for $\text{SrF}_2:10\text{Eu}$, and orange-red areas with the increase of Bi^{3+} content in $\text{SrF}_2:10\text{Eu}_x\text{Bi}_y$, showing the color tunability in the produced series (CIE values are listed in Table 5).

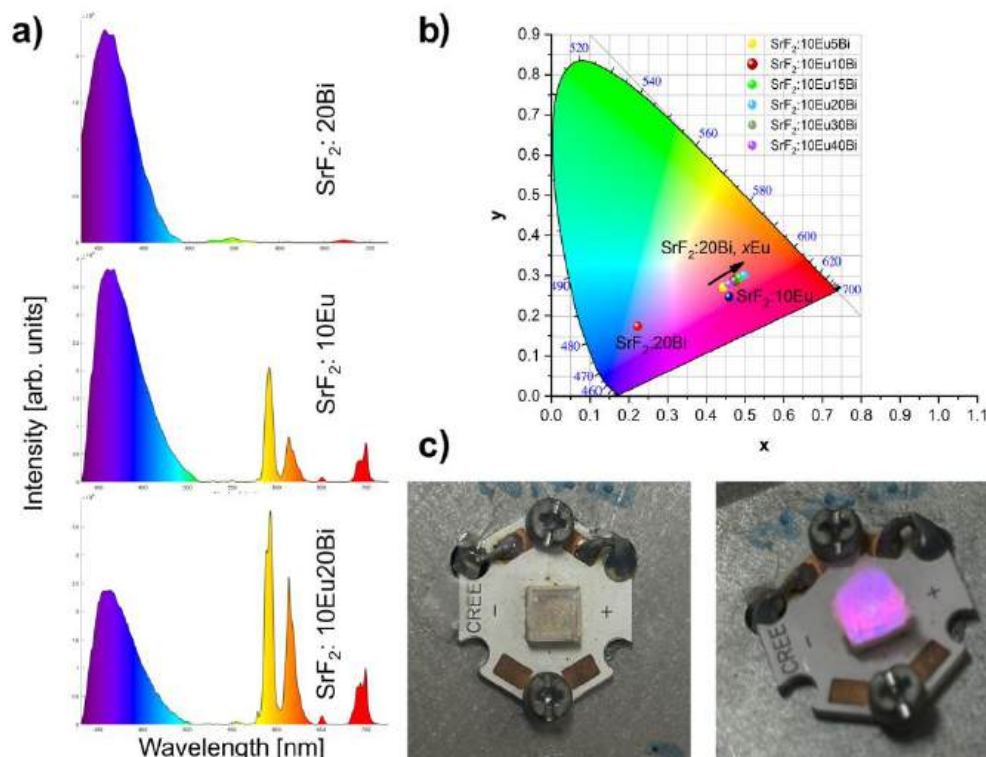


Figure 11. a) The room temperature PL emission spectra of $\text{SrF}_2:20\text{Bi}$, $\text{SrF}_2:10\text{Eu}$, and $\text{SrF}_2:10\text{Eu}20\text{Bi}$ samples showing both blue and red-light components in different ratios ($\lambda_{\text{exc}} = 265 \text{ nm}$), b) CIE chromaticity coordinates, and c) Fabricated LED device displaying pinkish violet light.

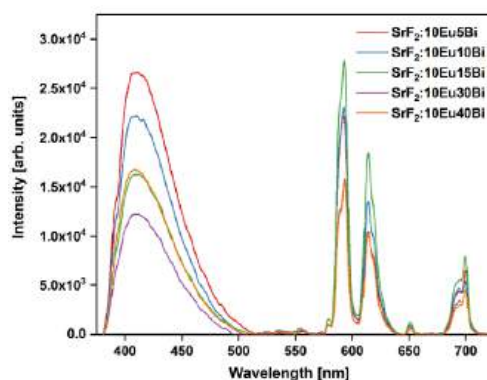


Figure 12 The room temperature PL emission spectra of $\text{SrF}_2:10\text{Eu}_x\text{Bi}_y$ ($x = 5, 10, 15, 30, \text{ and } 40$ mol%) samples measured in $380\text{--}725 \text{ nm}$ spectral range showing both blue and red-light components in different ratios ($\lambda_{\text{exc}} = 265 \text{ nm}$).

Balancing blue and red-light components is vital for optimizing plant health and maximizing yield in controlled environments. The integrated PL area in the $380\text{--}500 \text{ nm}$ (blue) and $575\text{--}725 \text{ nm}$ (red) wavelength range was used to determine the blue- and red-light emission portion. Table 5 shows that single-doped Bi^{3+} and Eu^{3+} SrF_2 exhibit strong blue emissions corresponding to the host material; however, increasing Bi^{3+} concentration enhances Eu^{3+} red emission in $\text{Eu}^{3+}/\text{Bi}^{3+}$ -activated samples. **The highest red/blue emission portion 40.8 : 59.2 was found for the sample $\text{SrF}_2:10\text{Eu}20\text{Bi}$.**

Table 5. Blue and red emission portions for the $\text{SrF}_2:20\text{Bi}$, $\text{SrF}_2:10\text{Eu}$, and $\text{SrF}_2:10\text{Eu}_x\text{Bi}$ ($x = 5, 10, 15, 20, 30$, and 40 mol%) samples.

Sample	% Blue	% Red	CIE (x, y) coordinates
$\text{SrF}_2:20\text{Bi}$	100.0	0.0	(0.223, 0.174)
$\text{SrF}_2:10\text{Eu}$	85.0	15.0	(0.399, 0.247)
$\text{SrF}_2:10\text{Eu}5\text{Bi}$	76.5	23.5	(0.444, 0.271)
$\text{SrF}_2:10\text{Eu}10\text{Bi}$	71.6	28.4	(0.474, 0.288)
$\text{SrF}_2:10\text{Eu}15\text{Bi}$	61.9	38.1	(0.486, 0.294)
$\text{SrF}_2:10\text{Eu}20\text{Bi}$	59.2	40.8	(0.498, 0.301)
$\text{SrF}_2:10\text{Eu}30\text{Bi}$	66.7	33.3	(0.473, 0.287)
$\text{SrF}_2:10\text{Eu}40\text{Bi}$	73.1	26.9	(0.459, 0.279)

Lastly, to demonstrate the potential application of the obtained material in LED fabrication, the powder sample with the highest emission intensity, $\text{SrF}_2:10\text{Eu}20\text{Bi}$, was mixed with a ceramic binder and placed on top of a 275 nm near-UV chip. Photographs of the fabricated LED device, presented in Figure 11c, display strong pinkish-violet light when the power supply is on.

The ability to convert UV into blue and red light in inorganic phosphors for LEDs in agricultural applications is essential to boost the photosynthesis of plants in greenhouses. For example, plants like tomatoes, peppers, and orchids benefit from red light during their flowering and fruiting stages. For plants like strawberries or cucumbers, red light will support better fruit production. Leafy greens like lettuce, spinach, and kale thrive under blue light as it promotes healthy leaf growth. Also, blue light helps young seedlings develop strong, healthy leaves and stems, giving them a solid start. Tunable red and blue light reported here in **Bi^{3+} -co-doped $\text{SrF}_2: \text{Eu}^{3+}$ nanoparticles could ensure plants receive the benefits of both types of light throughout their lifecycle.**

4. Properties of $\text{BaF}_2:\text{Eu}^{3+}$

4.1 Crystal structure of BaF_2 nanoparticles – WP1, sub-activity 1.3

To control the size and shape of nanoparticles, methods such as the emulsion/surfactant-assisted approach, along with adjustments in precursors and reaction conditions, are commonly employed. In this study, BaF_2 nanoparticles were synthesized using both microwave-assisted hydrothermal and solvothermal processes. Figure 12 displays the X-ray pattern of BaF_2 , referenced against the International Centre for Diffraction Data (ICDD) Card No. 01-085-1341. The X-ray diffraction analysis of the synthesized samples reveals that the solvothermal synthesis route exhibits more additional diffraction peaks than the hydrothermal method. However, the hydrothermally synthesized BaF_2 shows signs of contamination at 39° , 40.5° , and 47° Bragg angles, suggesting the need for optimization of temperature or reaction time. This research is still ongoing.

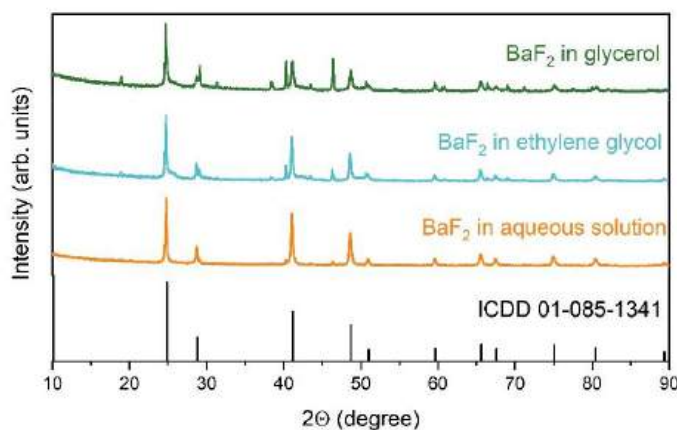


Figure 12. XRD patterns of BaF_2 powders synthesized via microwave route at $150\text{ }^\circ\text{C}$ for 10 min in water, ethylene glycol, and glycerol.

5. Properties of $\text{BaYF}_5:\text{Eu}^{3+}$ and $\text{BaYF}_5:\text{Bi}^{3+},\text{Eu}^{3+}$

5.1 PXRD and Morphology Analysis – WP1, sub-activity 1.3

Despite the addition of Eu^{3+} and Bi^{3+} ions, the main diffraction peaks of $\text{BYF}:x\text{Eu}$, $x = 1\text{--}20\text{ mol}\%$ (Figure 13a) and $\text{BYF}:10\text{Eu},y\text{Bi}^{3+}$, $y = 0\text{--}50\text{ mol}\%$ nanophosphors (Figure 13b), correspond to the main reflections from 111, 200, 220, 311, 222, 400, 331, 420, 422, and 511 crystal planes and resemble standard cubic data of ICDD No. 01-080-2728 for single-phase BaYF_5 , space group $Fm\bar{3}m$ (225). Compared to the standard cubic BaYF_5 , the magnified (111) diffraction peaks of $\text{BYF}:\text{Eu}$ samples are slightly shifted to the lower 2θ values due to the replacement of Y^{3+} ($r = 0.9\text{ \AA}$, ionic radii, VI coordinated) by a larger Eu^{3+} ($r = 0.947\text{ \AA}$, ionic radii, VI coordinated) as shown in Figure 13c. The magnified (111) diffraction peaks of $\text{BYF}:10\text{Eu},y\text{Bi}$ samples are shifted more to the lower 2θ values due to the replacement of Y^{3+} by two larger Eu^{3+} and Bi^{3+} ions ($r = 1.03\text{ \AA}$, ionic radii, VI coordinated) as shown in Figure 13d. Also, the degree of deviation in the shape of these diffraction peaks increases when the Bi^{3+} concentration exceeds 20 mol%, suggesting that high Bi^{3+} concentrations affect the crystal structure of the cubic BaYF_5 host lattice. Nonetheless, these results indicate that doping with a small amount of Bi^{3+} does not strongly affect the phase structure of BaYF_5 while higher doping concentrations distort BaYF_5 host lattice that, however, still resembles cubic. Figure 13e (left) shows that as the Eu^{3+} content increases, the unit cell volume in BYF fluctuates slightly. Figure 13e (right) shows a considerable increase in the unit cell volume of the $\text{BYF}:10\text{Eu},y\text{Bi}$ system as the Bi^{3+} concentration increases due to a larger distinction in Bi^{3+} and Y^{3+} ionic radius.

Table 6 shows the results of the structural analysis: crystallite size (CS), microstrain values, unit cell parameters, unit cell volume (CV), and data fit parameters (R_{wp} , R_p , R_e , GOF) of $\text{BYF}:10\text{Eu},y\text{Bi}$ ($y = 0, 5, 10, 20, 30,$ and $50\text{ mol}\%$) nanophosphors. The CS of $\text{BYF}:10\text{Eu}$ is estimated to be 19.6 nm, and the lattice constant a is 5.8925 \AA ($\text{CV} = 204.60\text{ \AA}^3$). The influence of Bi^{3+} doping in the $\text{BYF}:10\text{Eu}$ lattice causes crystal lattice expansion up to $a = 5.9942\text{ \AA}$, $\text{CV} = 215.37\text{ \AA}^3$ for the sample $\text{BYF}:10\text{Eu},50\text{Bi}$. As previously stated, expansion is expected when dopants with a larger ionic radius replace the Y^{3+} with a smaller ionic radius in BaYF_5 .

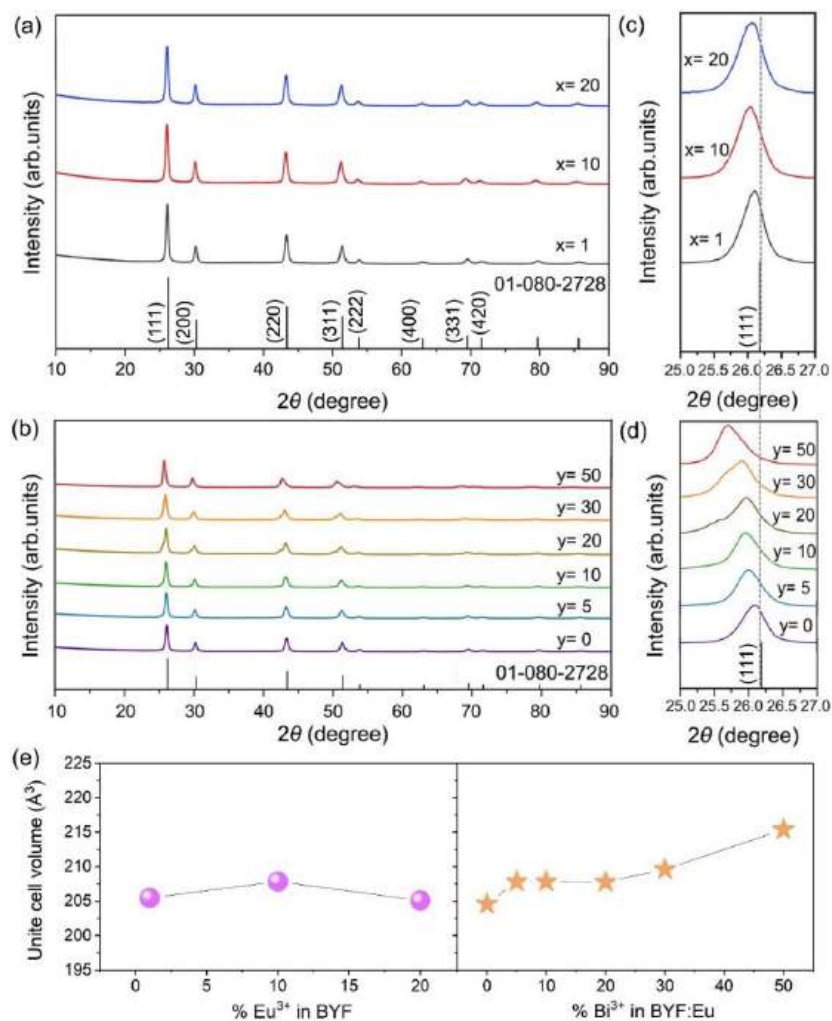


Figure 13. PXRD patterns of (a) BYF: $x\text{Eu}$ ($x = 1, 10,$ and 20 mol%) and (b) BYF:10Eu, $y\text{Bi}$ ($y = 0, 5, 10, 20, 30,$ and 50 mol%) nanoparticles; (c) The evolution of the (111) diffraction peak magnified from (a); (d) The evolution of the (111) diffraction peak magnified from (b); (e) The values of the unit cell volume versus Eu^{3+} and Bi^{3+} contents in BYF (purple circles) and BYF: 10Eu (orange stars), respectively.

Table 6. Results of the structural analysis of BYF: 10Eu, $y\text{Bi}$ nanophosphors, where $y = 0, 5, 10, 20, 30,$ and 50 mol% Bi^{3+}

Bi^{3+} content (mol%)	0	5	10	20	30	50
$a=b=c$ (Å)	5.8925 (3)	5.9236 (4)	5.9235 (5)	5.9227 (6)	5.9401 (6)	5.9942 (5)
CV Å ³	204.60 (4)	207.85 (5)	207.84 (6)	207.76 (7)	209.60 (7)	215.37 (6)
CS (Å)	196 (3)	274 (5)	305 (12)	198 (11)	100 (6)	95 (5)
Strain	0.46 (3)	0.64 (2)	0.75 (2)	1.03 (6)	0.23 (3)	0.26 (3)
GOF	1.1254	1.5272	1.6212	1.6678	2.9693	3.6494
* R_{wp}	4.23	5.79	6.14	6.42	11.08	13.43
** R_p	3.16	4.45	4.66	4.95	7.57	8.71
*** R_e	3.75	3.79	3.78	3.85	3.73	3.68

* R_{wp} —the weighted profile factor; ** R_p —the profile factor; *** R_e —the expected weighted profile factor; GOF—the goodness of fit.

Figure 14 shows SEM images of BYF:10Eu phosphor nanoparticles with a particle size distribution. Nanoparticles are of a quasispherical shape, as well as a high degree of crystallinity. The average

crystalline size of BYF: 10Eu nanoparticles, considering more than 100 particles, was estimated to be 33 ± 2 nm (see Figure 14c). The average particle size was calculated without considering partially displayed particles. The histogram was fitted using a lognormal distribution.

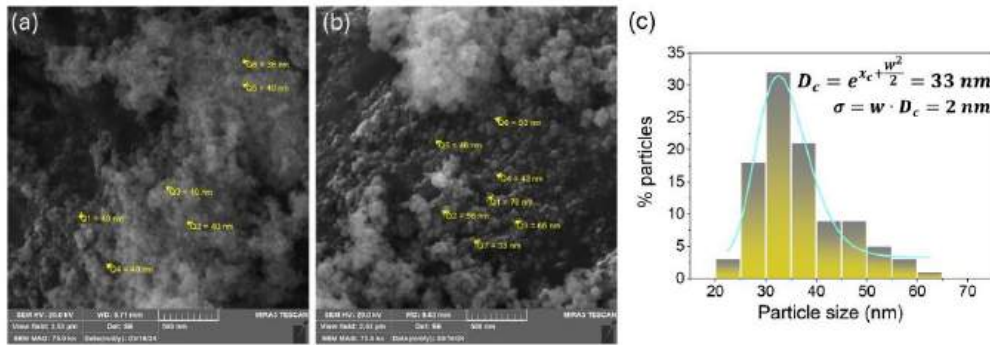


Figure 14. (a, b) SEM images of solvothermally synthesized BYF: 10Eu phosphor nanoparticle; (c) The particle size distribution.

5.2 Spectroscopic Properties – WP1, sub-activity 1.3

Figure 16a shows the room temperature diffuse reflectance spectra of BYF:10Eu, y Bi ($y = 0, 5, 10, 20, 30,$ and 50 mol%) samples in the 220–500 nm wavelength range. The spectra reveal the absorption band of Eu³⁺ at 394 nm, originating from the ground state 7F_0 to the upper level 5L_6 transition. In addition, it is observed that the UV band edge tends to shift towards lower energy with an increase of Bi³⁺ content in the BYF: Eu. This red shift with the change of Bi³⁺ content indicates a strong absorption of Bi³⁺, which lies in the UV region. The spectroscopic properties of a representative Bi³⁺ co-doped BYF: 10Eu phosphor are analyzed, whereas Figure 15 shows the photoluminescence excitation and emission spectra of Bi-free BYF with varying Eu³⁺ contents. The room temperature photoluminescence excitation spectra of all BYF: Eu, Bi samples recorded in the 250–330 nm ($\lambda_{em} = 698$ nm) wavelength range are given in Figure 16b. The intense peaks at 297 and 317 nm correspond to the $^7F_0 \rightarrow ^5F_1$ and $^7F_0 \rightarrow ^5H_1$ transitions of Eu³⁺, respectively. A red shift is also observed with increasing Bi³⁺ content. This suggests that Bi³⁺ may act as a sensitizer, broadening the Eu³⁺ absorption spectrum response and increasing the luminous intensity of Eu³⁺.

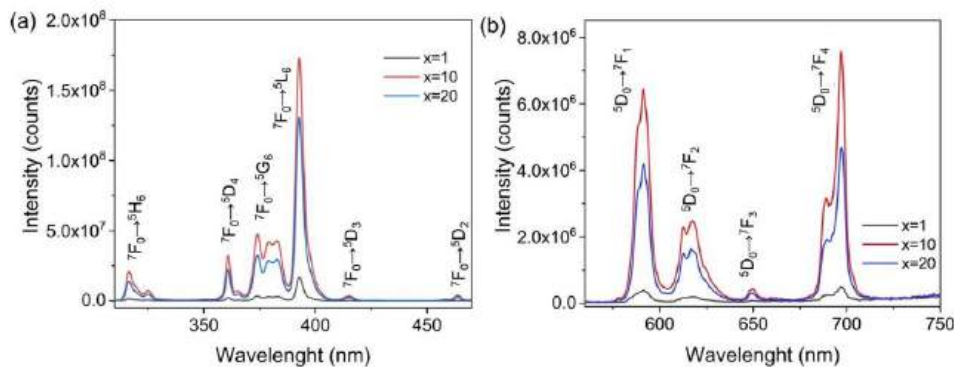


Figure 15. Room temperature photoluminescence for all BYF: x Eu ($x = 1, 10,$ and 20 mol%) samples: (a) Excitation spectra under $\lambda_{em} = 592$ nm; (b) Emission spectra under $\lambda_{ex} = 391$ nm;

The photoluminescence emission spectra of all BYF: Eu, Bi samples recorded at room temperature are displayed in Figure 16c ($\lambda_{ex} = 265$ nm). All emissions correspond to $4f-4f$ transitions of Eu³⁺ are

located at ~ 594 nm (${}^5\text{D}_0 \rightarrow {}^7\text{F}_1$), ~ 613 nm (${}^5\text{D}_0 \rightarrow {}^7\text{F}_2$), ~ 650 nm (${}^5\text{D}_0 \rightarrow {}^7\text{F}_3$), and ~ 700 nm (${}^5\text{D}_0 \rightarrow {}^7\text{F}_4$). The emission in the deep-red spectral region around 700 nm, corresponding to the ${}^5\text{D}_0 \rightarrow {}^7\text{F}_4$ transition, exhibits the highest intensity in these spectra. This is not common for Eu^{3+} , but it has been reported for several hosts where the structural distortion from octahedral symmetry to non-centrosymmetric D_{4d} exists [37,38], as odd-rank components of the static forced electric dipole and ligand polarizability-dependent dynamic coupling mechanisms are high, particularly in the highly polarizable chemical environment [39]. Figure 16d shows that europium's photoluminescent intensity continually increases until the Bi^{3+} content reaches 20 mol%, while the further addition of Bi^{3+} decreases the emission intensity. The integrated emission intensity in the 520 – 720 nm wavelength range shows that the representative BYF: 10Eu, 20Bi sample has a 216% emission enhancement compared to the Bi-free BYF: 10Eu phosphor. Figure 16e shows the translucent white color of representative BYF: 10Eu, 20Bi phosphor nanoparticles under daylight (left) and the red appearance under UV light (right).

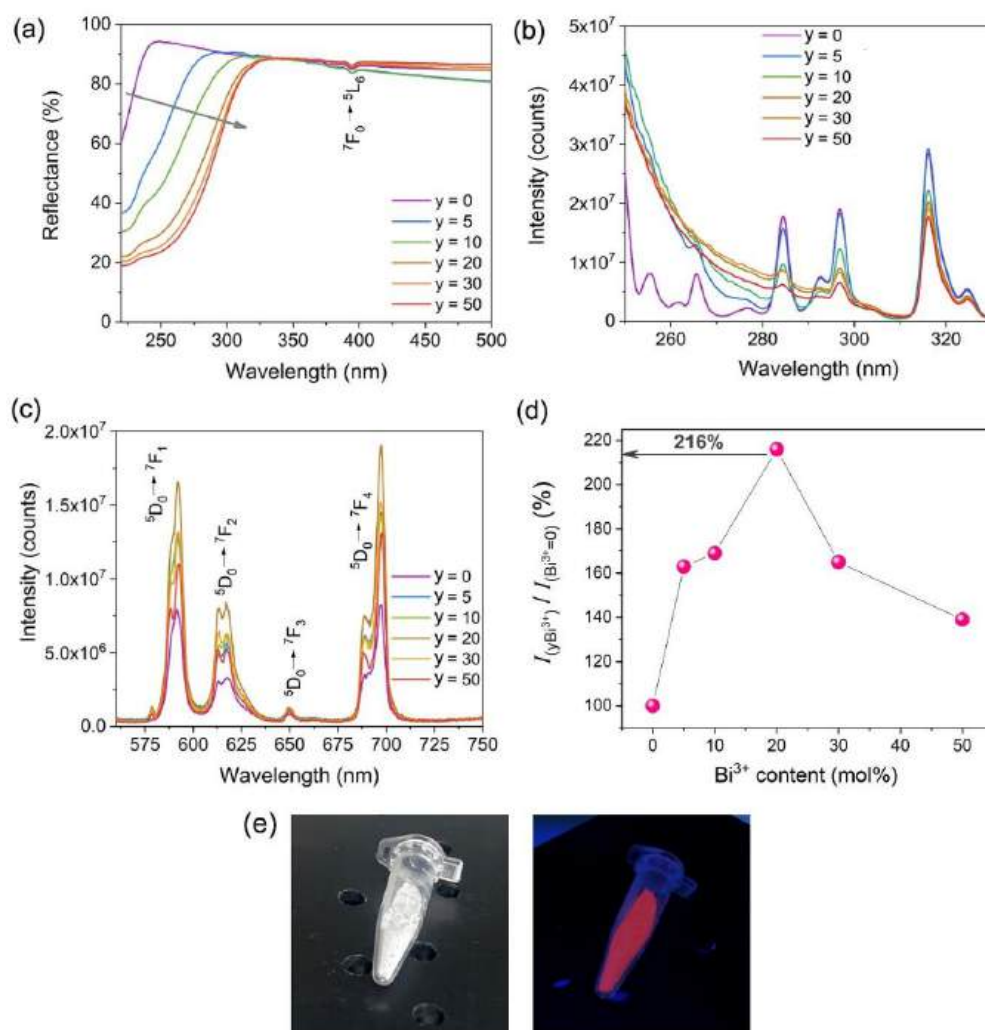


Figure 16. (a) Room temperature diffuse reflectance spectra for BYF: 10Eu, $y\text{Bi}$ ($y = 0, 5, 10, 20, 30,$ and 50 mol%) samples; Room temperature photoluminescence for BYF: 10Eu, $y\text{Bi}$ ($y = 0, 5, 10, 20, 30,$ and 50 mol%) samples: (b) Excitation spectra under $\lambda_{em} = 698$ nm; (c) Emission spectra under $\lambda_{ex} = 265$ nm; (d) Ratio of the integrated emission intensity for BYF: 10Eu samples with varied Bi concentration and Bi-free BYF: 10Eu sample as a function of Bi^{3+} ions concentration; (e) The appearance of representative BYF: 10Eu, 20Bi phosphor nanoparticles under daylight (left) and UV light (right).

5.3 Energy transfer in BYF: Bi Eu, phosphor nanoparticles – WP1, sub-activity 1.3

The third set of BYF samples with constant Bi^{3+} ($y = 20$ mol%) and various Eu^{3+} ($x = 1, 5, 10, 20$ mol%) contents were prepared to examine the energy transfer mechanism from a sensitizer to an activator. Figure 17 with the XRD spectra confirms the phase purity of these samples.

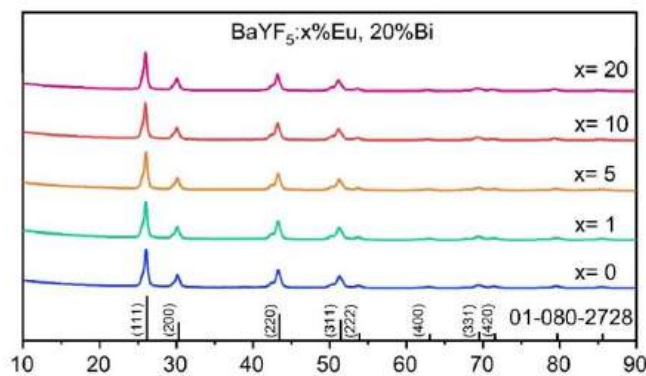


Figure 17. PXRD patterns of BYF: $x\text{Eu}$, 20Bi ($x = 0, 1, 5, 10,$ and 20 mol%) phosphor nanoparticles.

Figures 18a and 18b show the photoluminescence spectra of BYF nanoparticles with constant 20 mol% Bi and different Eu ($x = 1, 5, 10,$ and 20 mol%) concentrations. The photoluminescent spectra of BYF: Bi, Eu phosphors revealed a broadband blue emission centered at approximately 430 nm attributed to the $^3\text{P}_1 \rightarrow ^1\text{S}_0$ allowed Bi^{3+} transition. These Figures also show that $\text{Bi}^{3+} \rightarrow \text{Eu}^{3+}$ energy transfer in the BYF: $x\text{Eu}$, 20Bi ($x = 1, 5, 10,$ and 20 mol%) system has a different character, depending on Bi^{3+} content.

Energy transfer from a sensitizer to an activator can occur *via* radiative transfer, exchange interaction, or multipole-multipole interaction. Dips in the sensitizer's emission spectra that correlate to the absorption spectrum of activated ions demonstrate the possibility of radiative energy transfer from the sensitizer to the activator. As shown in Figure 18b, the emission spectra of BYF: 20Bi , 20Eu clearly show a dip that overlaps with the absorption of Eu^{3+} , indicating that the energy transfer has a radiative character. On the other hand, Figure 18a reveals that $20\text{mol}\%$ Bi^{3+} and Eu^{3+} concentrations less than or equal to 10 mol% contribute to a non-radiative character of energy transfer in BYF: Bi, Eu.

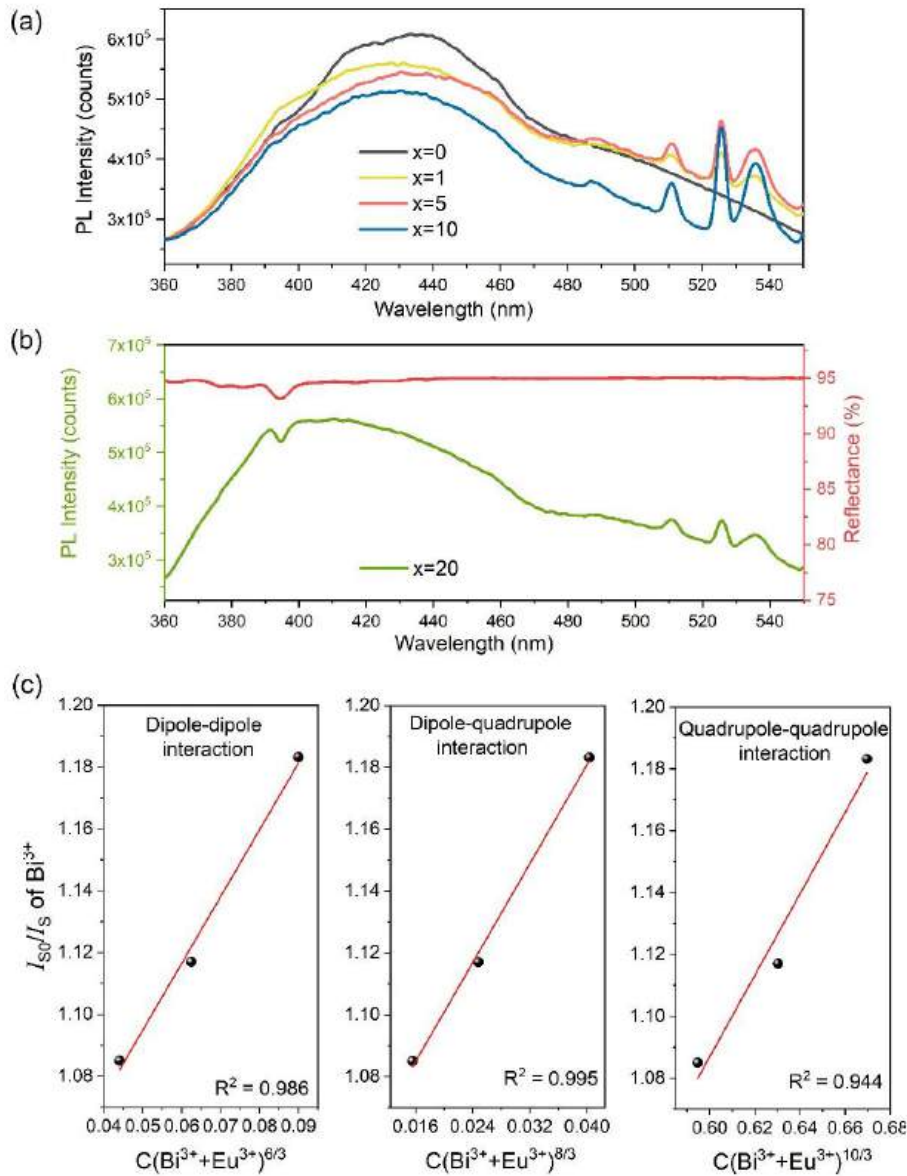


Figure 18. (a) The emission spectra of BYF: xEu, 20Bi (x = 0, 1, 5, and 10 mol%) nanoparticles; (b) Overlap of the emission spectrum of BYF: 20Eu, 20Bi and absorption of BYF: 10Eu; (c) Plots of I_{sq}/I_s versus C(Bi³⁺+Eu³⁺)^{6/3}, C(Bi³⁺+Eu³⁺)^{8/3} and C(Bi³⁺+Eu³⁺)^{10/3}.

According to the Dexter and Schulman theory, concentration quenching in inorganic phosphors occurs when energy passes from one activator to another, often until the energy sink in the lattice is achieved. Blasse reported that the average separation distance between the sensitizer and activator ions is equal to the critical distance R_c , which can be expressed as follows:

$$R_c \approx 2 \left(\frac{3V}{4\pi C_{Bi+Eu} N} \right)^{1/3}, \quad (1)$$

where N is the number of sites that lanthanide ions occupy per unit cell, V is the unit cell volume, and C_{Bi+Eu} is the overall doping concentration of the Bi³⁺ and Eu³⁺ ions. For BaYF₅, $N = 2$ and $V = 204.34 \text{ \AA}^3$. Using Eq. (1), R_c is determined to be 9.8, 9.2, and 8.7 Å for $C_{Bi+Eu} = 0.21, 0.25,$ and 0.30 , respectively. The critical concentration of C_{Bi+Eu} in the BYF host is 0.30, while higher concentrations show emission-quenching effects.

Non-radiative energy transfers include exchange interaction and multipole-multipole

interaction. Exchange interaction occurs when the sensitizer and activator are separated by less than 5 Å and their orbitals overlap significantly. In our case, the critical distance between Bi³⁺ and Eu³⁺ is 8.7 Å, which excludes energy transfer *via* exchange interactions. Therefore, electric multipole-multipole interaction is a potential energy transfer mechanism in BYF: Bi, Eu nanophosphors when Bi³⁺ content is less than or equal to 10 mol%. Based on the Förster Resonance Energy Transfer formula of multipolar interaction and Reisfeld's approximation, the following relation can be given:

$$\frac{\eta_0}{\eta} \approx \frac{I_{S0}}{I_S} \propto C_{Bi+Eu}^{n/3} \quad (2)$$

where η_0 and I_{S0} represent the emission quantum efficiency and luminescence intensity of the Bi³⁺ sensitizer ions alone, while η and I_S are the emission quantum efficiency and luminescence intensity of Bi³⁺ in the presence of Eu³⁺ activator ions. C_{Bi+Eu} is the overall doping concentration of the Bi³⁺ and Eu³⁺ ions, and $n = 6, 8, \text{ or } 10$ reflect dipole-dipole, dipole-quadrupole or quadrupole-quadrupole interactions, respectively. Eq. (2) shows that the luminosity ratio I_{S0}/I_S can be used to estimate the amount of η_{S0}/η_S . Figure 18c depicts the linear plots between I_{S0}/I_S and $C_{Bi+Eu}^{n/3}$ in all cases of electric multipole-multipole interaction. A good linear trend for $n=8$ ($C_{Bi+Eu}^{8/3}$) shows that dipole-quadrupole interaction is the dominant mechanism for energy transfer from Bi³⁺ to Eu³⁺ in BYF phosphor nanoparticles.

The energy transfer efficiency (η_T) from a sensitizer to an activator ion can be calculated by the following relation:

$$\eta_T = 1 - \frac{I_S}{I_{S0}} \quad (3)$$

Energy transfer efficiencies (η_T) of as-prepared samples increases with the increase of Eu³⁺ content, with maximum values of 16% for the representative BYF: 10Eu, 20Bi sample.

6. Properties of BaGdF₅:Bi³⁺,Eu³⁺

6.1 Structure and optical properties of Bi³⁺,Eu³⁺ co-doped BaGdF₅ nanoparticles – WP3, sub-activity 1.3

Figure 19 shows the room temperature diffuse reflectance spectra of BaGdF₅:10Eu and BaGdF₅:10Eu,5Bi samples in the 220–1200 nm wavelength range. The spectra reveal the absorption band of Eu³⁺ at 394 nm, originating from the ground state ⁷F₀ to the upper level ⁵L₆ transition. In addition, it is observed that the UV band edge tends to shift towards lower energy with the addition of Bi³⁺ content in the BaGdF₅:10Eu. This red shift indicates a strong absorption of Bi³⁺, which lies in the UV region.

Figure 20-left shows the photoluminescence excitation and emission spectra of BaGdF₅:10Eu,5Bi, recorded in the 360–560 nm ($\lambda_{em} = 592$ nm) wavelength range. The room temperature photoluminescence emission spectra, recorded in the wavelength range 550 – 750 nm, are displayed in Figure 20-right ($\lambda_{ex} = 265$ nm). All emissions correspond to 4f–4f transitions of Eu³⁺ are located at ~594 nm (⁵D₀ → ⁷F₁), ~613 nm (⁵D₀ → ⁷F₂), ~650 nm (⁵D₀ → ⁷F₃), and ~700 nm (⁵D₀ → ⁷F₄). The emission in the deep-red spectral region around 700 nm exhibit the highest intensities in spectra. This is not common for Eu³⁺, but it has been reported for several hosts where the structural distortion from octahedral symmetry to non-centrosymmetric D_{4d} exists, as odd-rank components of the static forced electric dipole and ligand polarizability-dependent dynamic coupling mechanisms are high, particularly in the highly polarizable chemical environment. The detail analysis of Bi³⁺ cooping BaGdF₅:10mol%Eu³⁺ nanophosphor is still ongoing.

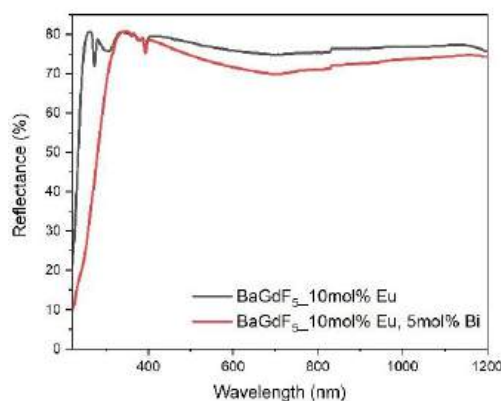


Figure 19. Room temperature diffuse reflectance spectra of $\text{BaGdF}_5:10\text{Eu}$ and $\text{BaGdF}_5:10\text{Eu},5\text{Bi}$ samples

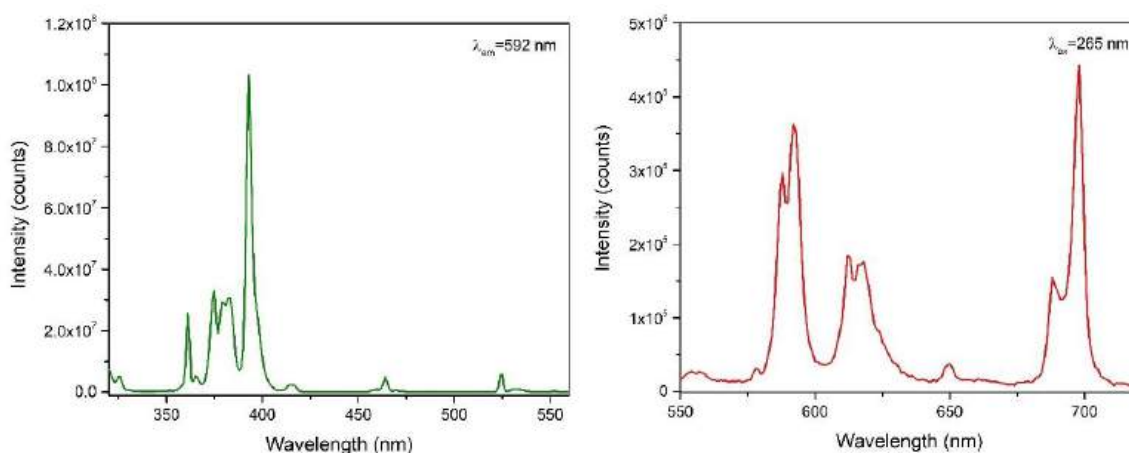


Figure 20. Room temperature photoluminescence excitation (left) and emission (right) spectra of $\text{BaGdF}_5:10\text{Eu},5\text{Bi}$

7. Properties of $\text{RbY}_3\text{F}_{10}:\text{Eu}^{3+}$

7.1 Structure and morphology of Eu^{3+} -doped $\text{RbY}_3\text{F}_{10}$ nanoparticles – WP1, sub-activity 1.3

Figure 21 shows the X-ray pattern of prepared undoped $\text{RbY}_3\text{F}_{10}$ presented with the International Centre for Diffraction Data (ICDD) Card No. 01-085-9553. To optimize the synthesis procedure, different chelating agents were used and showed: (i) without chelating agents, an additional diffraction corresponding from RbY_2F_7 is observed, (ii) using citric acid and pH values below 6, YF_3 phase is observed, (iii) using ethylenediaminetetraacetic acid (EDTA) in molar ratio 1:1 (EDTA:Re) and pH values below 9, additional diffraction peaks were observed, and (iv) using ethylenediamine acid (EDTA) in molar ratio 1:6 (EDTA:Re) and pH values below 9, additional diffraction peaks were observed. The optimized sample was obtained using a molar ratio of 1:6 (EDTA:Re) and pH values above 6. The X-ray diffraction examination of the optimized samples proved a single phase with cF112 (225) space group (phase prototype: KY_3F_{10}). Traces of contamination or other phase peaks were not observed, indicating

that the pure $\text{RbY}_3\text{F}_{10}$ crystal structure. The three-dimensional schematic view of the $\text{RbY}_3\text{F}_{10}$ crystal structure is shown in Figure 21 (down) built via *Diamond 3.2* software.

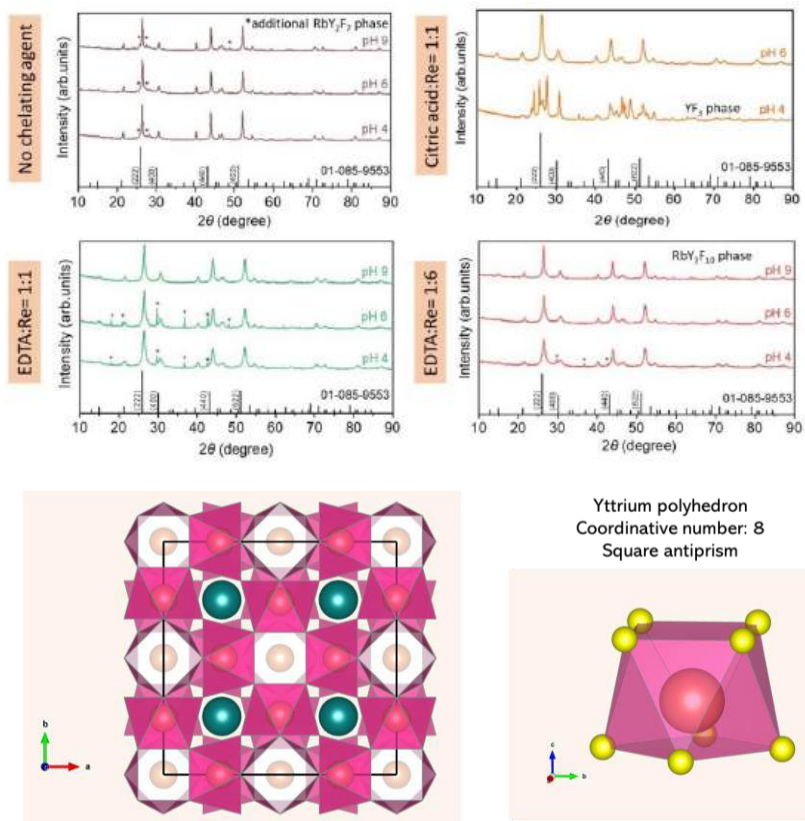


Figure 21. PXRD patterns of $\text{RbY}_3\text{F}_{10}$ nanoposphors prepared via different chelating agents and the three-dimensional schematic view of the crystal structure.

Figure 22 shows SEM images of $\text{RbY}_3\text{F}_{10}$ phosphor nanoparticles synthesized using different chelating agents. Nanoparticles are spherical, as well as having a high degree of crystallinity. The average crystalline size of $\text{RbY}_3\text{F}_{10}$ nanoparticles was estimated to be in the range between 50 and 90 nm.

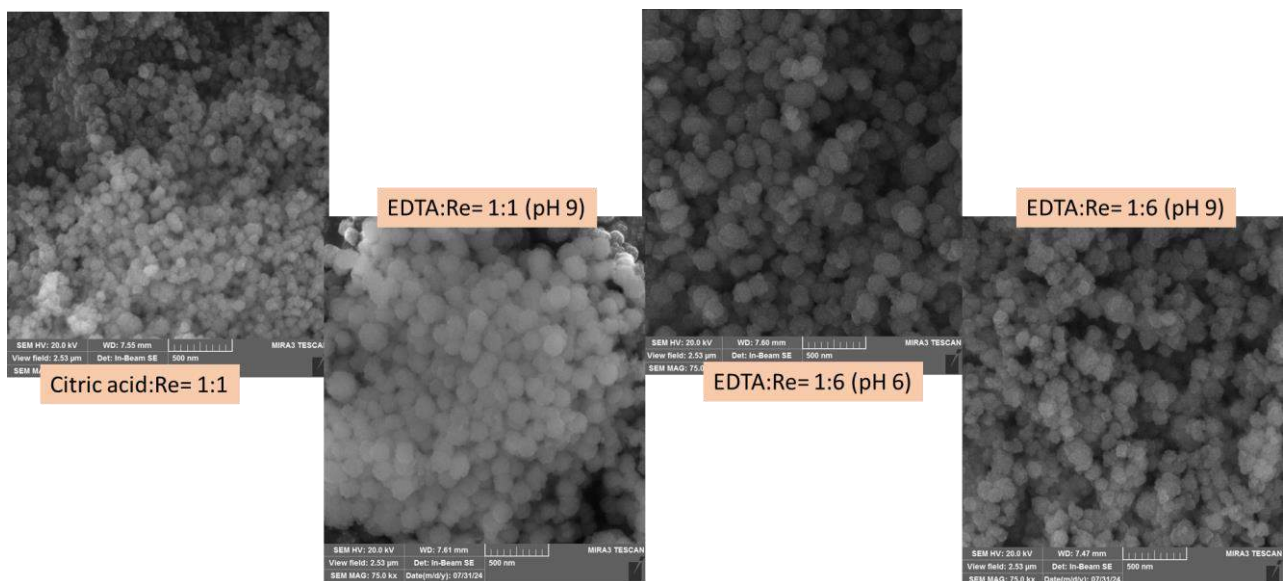


Figure 22. SEM images of synthesized $\text{RbY}_3\text{F}_{10}$ phosphor nanoparticle.

7.2 Photoluminescence of Eu^{3+} -doped $\text{RbY}_3\text{F}_{10}$ nanoparticles – WP1, sub-activity 1.3

The room temperature photoluminescence spectra of $\text{RbY}_3\text{F}_{10}:10 \text{ mol}\% \text{Eu}^{3+}$ synthesized using different chelating agents are presented in Figure 23. The most intense Eu^{3+} emission is observed for the sample prepared using EDTA as a chelating agent and $\text{pH}=9$, therefore, this synthesis route was used for the optimization of Eu^{3+} content in $\text{RbY}_3\text{F}_{10}$ nanophosphor. Figure 24. (left) shows the X-ray pattern of prepared undoped $\text{RbY}_3\text{F}_{10}:\text{xEu}^{3+}$ ($x = 0, 1, 5, 10, 30, 50,$ and $75 \text{ mol}\%$) presented with the International Centre for Diffraction Data (ICDD) Card No. 01-085-9553. The XRD of the sample doped with $75 \text{ mol}\%$ of Eu^{3+} displays a few additional peaks. This observation indicates that the high amount of Eu^{3+} leads to the crystallization of an additional compound to pure-phase $\text{RbY}_3\text{F}_{10}$. Therefore, Eu^{3+} co-doping of $\text{RbY}_3\text{F}_{10}$ is possible for Eu^{3+} concentrations equal to or less than $50 \text{ mol}\%$. The photoluminescence emission spectra of all $\text{RbY}_3\text{F}_{10}:\text{xEu}^{3+}$ ($x = 1, 5, 10, 30,$ and $50 \text{ mol}\%$) samples recorded at room temperature are displayed in Figure 24 (right, $\lambda_{\text{ex}} = 405 \text{ nm}$). All emissions correspond to $4f-4f$ transitions of Eu^{3+} are located at $\sim 594 \text{ nm}$ ($^5\text{D}_0 \rightarrow ^7\text{F}_1$), $\sim 613 \text{ nm}$ ($^5\text{D}_0 \rightarrow ^7\text{F}_2$), $\sim 650 \text{ nm}$ ($^5\text{D}_0 \rightarrow ^7\text{F}_3$), and $\sim 700 \text{ nm}$ ($^5\text{D}_0 \rightarrow ^7\text{F}_4$). Europium ions' emission intensity monotonically increases in the co-doped samples up to $50 \text{ mol}\%$ of Eu^{3+} . These findings suggest that highly doped $\text{RbY}_3\text{F}_{10}:\text{Eu}^{3+}$ nanophosphors, exhibiting strong red and deep red emissions, are promising candidates for plant-targeted LEDs. Consequently, our future research will focus on a detailed analysis of Bi^{3+} co-doping in $\text{RbY}_3\text{F}_{10}:\text{Eu}^{3+}$ nanophosphors to improve absorption in the blue spectral range.

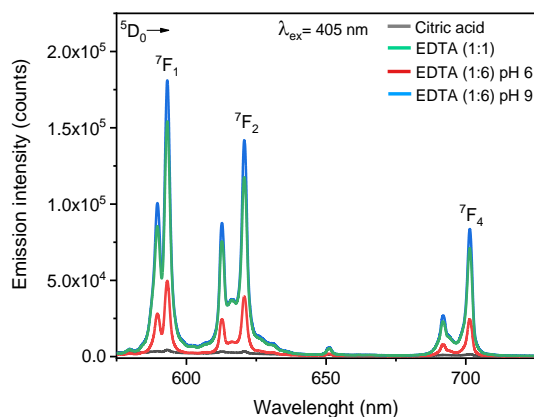


Figure 23. Room temperature emission spectra of $\text{RbY}_3\text{F}_{10}:10 \text{ mol}\% \text{Eu}^{3+}$ using different chelating agents recorded under $\lambda_{\text{ex}} = 405 \text{ nm}$.

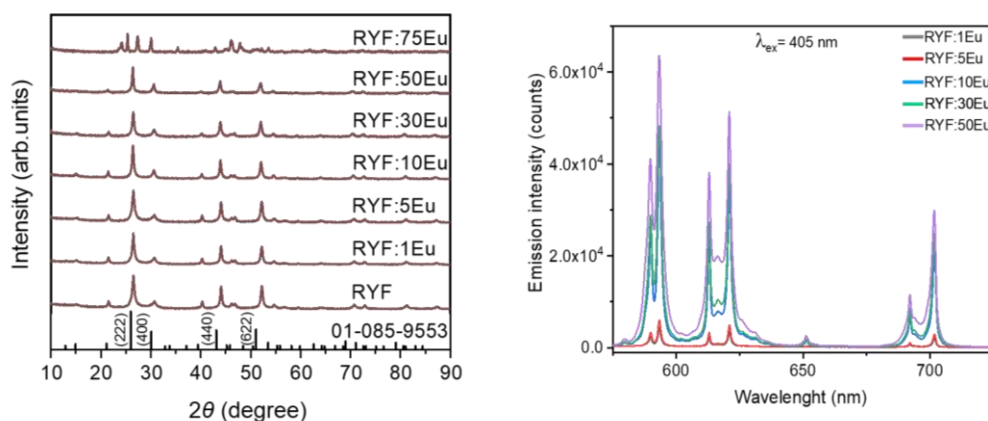


Figure 24. PXRD patterns of $\text{RbY}_3\text{F}_{10}:\text{xEu}^{3+}$ ($x = 0, 1, 5, 10, 30, 50,$ and $75 \text{ mol}\%$) nanophosphors (left) and room temperature emission spectra of $\text{RbY}_3\text{F}_{10}:\text{xEu}^{3+}$ ($x = 1, 5, 10, 30,$ and $50 \text{ mol}\%$) recorded under $\lambda_{\text{ex}} = 405 \text{ nm}$.

Additionally, a large band gap of approximately 9 eV has been observed for the fluoride host $\text{RbY}_3\text{F}_{10}:\text{Eu}^{3+}$, as shown in Figure 25. This value aligns with literature data for other fluoride hosts, such as K_2SiF_6 and K_2TiF_6 , which have band gaps around 8 eV.

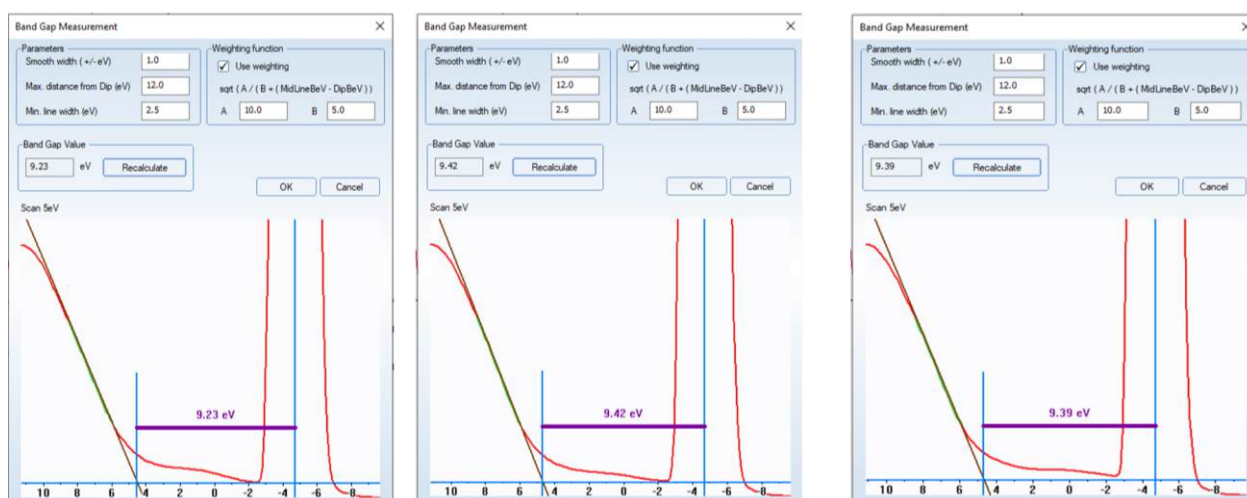


Figure 25. Band gap calculation of $\text{RbY}_3\text{F}_{10}:\text{10mol}\%\text{Eu}^{3+}$.

8. Properties of $\text{GdF}_3:\text{Bi}^{3+},\text{Eu}^{3+}$

8.1 Structural and optical properties of Eu^{3+} -doped GdF_3 nanoparticles – WP1, sub-activity 1.1

Figure 26 (left) shows the X-ray pattern of prepared $\text{GdF}_3:\text{xEu}$ ($\text{x} = 5, 10, 15, 20,$ and $30 \text{ mol}\%$). Traces of contamination or other phase peaks were not observed, indicating that dopant Eu^{3+} ions were embedded into the GdF_3 lattice. The room temperature photoluminescence spectra of $\text{GdF}_3:\text{xEu}$ ($\text{x} = 5, 10, 15, 20,$ and $30 \text{ mol}\%$), recorded in the wavelength range $540 - 720 \text{ nm}$, shows that optimal Eu^{3+} content is $20 \text{ mol}\%$ ($\lambda_{\text{ex}} = 393 \text{ nm}$). Europium's photoluminescent intensity increases until the Eu^{3+} content reaches $20 \text{ mol}\%$, while the further addition of Eu^{3+} decreases the emission intensity. Therefore, the representative/optimized sample $\text{Gd}_{0.8}\text{Eu}_{0.2}\text{F}_3$ was co-doped with Bi^{3+} ions. Figure 26 (right) shows that all emissions corresponding to $4f-4f$ transitions of Eu^{3+} are located at $\sim 594 \text{ nm}$ (${}^5\text{D}_0 \rightarrow {}^7\text{F}_1$), $\sim 613 \text{ nm}$ (${}^5\text{D}_0 \rightarrow {}^7\text{F}_2$), $\sim 650 \text{ nm}$ (${}^5\text{D}_0 \rightarrow {}^7\text{F}_3$), and $\sim 700 \text{ nm}$ (${}^5\text{D}_0 \rightarrow {}^7\text{F}_4$). The europium emission intensity monotonically decreases in the co-doped samples up to $10 \text{ mol}\%$ of Bi^{3+} . We may conclude that energy transfer from Bi^{3+} to Eu^{3+} is not observed in the $\text{Gd}_{0.8}\text{Eu}_{0.2}\text{F}_3$ nanophosphor.

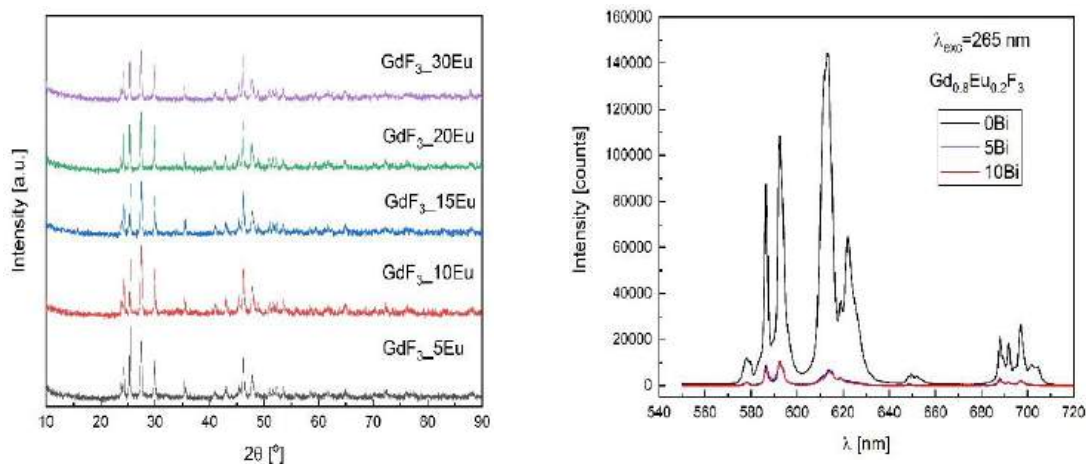


Figure 26. XRD patterns of $\text{LuF}_3:\text{xEu}$ ($x = 5, 10, 15,$ and $20 \text{ mol}\%$) samples presented with the ICDD card No. 00-032-0612. The room temperature photoluminescence spectra of $\text{LuF}_3:\text{xEu}$ ($x = 5, 10, 15,$ and $20 \text{ mol}\%$) samples.

9. Properties of $\text{LuF}_3:\text{Eu}^{3+}$

9.1 Structure analysis of Eu^{3+} -doped LuF_3 – WP1, sub-activity 1.3

Figure 27 shows the X-ray pattern of $\text{LuF}_3:\text{xEu}$ ($x = 5, 10, 15,$ and $20 \text{ mol}\%$) presented with the International Centre for Diffraction Data (ICDD) Card No. 00-032-0612. The X-ray diffraction examination of the synthesized samples proved a single phase in agreement with the orthorhombic $Pm\bar{m}a$ structure of LuF_3 . Traces of contamination or other phase peaks were not observed in either set of samples, indicating that dopant Eu^{3+} ions were embedded into the LuF_3 lattice. Table 7 shows the results of the structural analysis: crystallite size (CS), microstrain values, unit cell parameters, unit cell volume (CV), and data fit parameters (R_{wp} , R_p , R_e , GOF) of $\text{LuF}_3:\text{xEu}$ nanophosphors. The CS of $\text{LuF}_3:\text{xEu}$ are in the range between 18,4 and 25,1 nm. The influence of Eu^{3+} doping in the LuF_3 lattice causes crystal lattice expansion up to $a = 6.2176 \text{ \AA}$, $a = 6.8061 \text{ \AA}$, and $a = 4.4589 \text{ \AA}$ for the sample prepared with 20 mol% Eu^{3+} content. As previously stated, expansion is expected when dopants with a larger ionic radius replace the Lu^{3+} with a smaller ionic radius in LuF_3 .

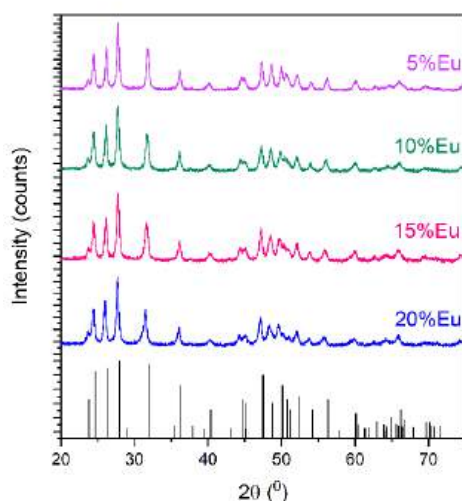


Figure 27. XRD patterns of $\text{LuF}_3:\text{xEu}$ ($x= 5, 10, 15,$ and 20 mol%) samples presented with the ICDD card No. 00-032-0612.

Table 7. Results of the structural analysis of $\text{LuF}_3:\text{xEu}$ nanophosphors, where $x = 5, 10, 15,$ and 20 mol% Eu^{3+}

ICDD 00-032-0612	$\text{LuF}_3:5\text{Eu}$	$\text{LuF}_3:10\text{Eu}$	$\text{LuF}_3:15\text{Eu}$	$\text{LuF}_3:20\text{Eu}$
CS (A)	193 (7)	208 (3)	184(17)	251(5)
Strain	0.13 (3)	0.33 (3)	0.213(5)	0.43(3)
GOF	2.1936	1.7154	1.8069	1.6841
Rwp	15.39%	14.08%	12.82%	11.65%
Rp	11.30%	10.72%	9.55%	8.78%
Re	7.02%	8.21%	7.09%	6.92%
a	6.1585(11)	6.1773(14)	6.2045(13)	6.2176(15)
b	6.7757(13)	6.7829 (15)	6.7997(14)	6.8061(17)
c	4.4836(9)	4.4733(11)	4.4734(10)	4.4589(12)

9.2 Photoluminescence spectra of Eu^{3+} -doped LuF_3 – WP1, sub-activity 1.3

The room temperature photoluminescence spectra, recorded in the wavelength range 500 – 750 nm, are displayed in Figure 28 ($\lambda_{\text{ex}} = 393$ nm). All emissions correspond to $4f-4f$ transitions of Eu^{3+} are located at ~ 594 nm (${}^5\text{D}_0 \rightarrow {}^7\text{F}_1$), ~ 613 nm (${}^5\text{D}_0 \rightarrow {}^7\text{F}_2$), ~ 650 nm (${}^5\text{D}_0 \rightarrow {}^7\text{F}_3$), and ~ 700 nm (${}^5\text{D}_0 \rightarrow {}^7\text{F}_4$). The emission in the orange around 594 nm and deep-red spectral region around 700 nm exhibit the highest intensities in these spectra. This is not common for Eu^{3+} , but it has been reported for several hosts where the structural distortion from octahedral symmetry to non-centrosymmetric D_{4d} exists, as odd-rank components of the static forced electric dipole and ligand polarizability-dependent dynamic coupling mechanisms are high, particularly in the highly polarizable chemical environment. Figure 15 shows that europium's photoluminescent intensity increases until the Eu^{3+} content reaches 10 mol%, while the further addition of Eu^{3+} decreases the emission intensity. Our future work will focus on the detail analysis of Bi^{3+} cooping $\text{LuF}_3:10\text{mol}\%\text{Eu}^{3+}$ nanophosphor.

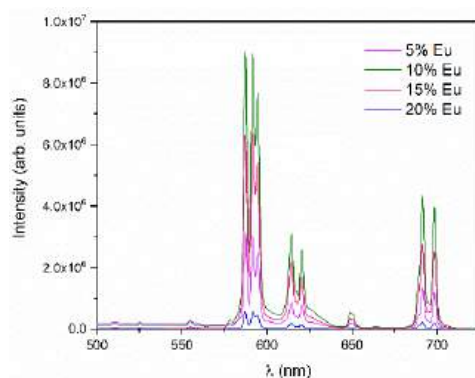


Figure 28. The room temperature photoluminescence spectra of $\text{LuF}_3:\text{xEu}$ ($\text{x} = 5, 10, 15, \text{ and } 20 \text{ mol\%}$) samples.

10. Scientific Publications and Peer-Reviewed Journals

During the first year of the project implementation, the LEDtech-GROW team achieved the following: three papers were published in peer-reviewed journals, all of which are Open Access as per the grant agreement; four poster presentations were delivered at international conferences; and one invited talk was given at a domestic conference.

1. B. Milićević, A. Ćirić, Z. Ristić, M. Medić, A. N. Alodhayb, I. Radosavljević Evans, Ž. Antić, M. D. Dramićanin. "Eu³⁺-activated Sr₂GdF₇ colloid and nano-powder for horticulture LED applications". *Journal of Alloys and Compounds* 1010 (5) (2025) 177820. <https://doi.org/10.1016/j.jallcom.2024.177820>
2. K. Milenković, Lj. Đačanin Far, S. Kuzman, Ž. Antić, A. Ćirić, M. D. Dramićanin, B. Milićević. "Red emission enhancement in BaYF₅:Eu³⁺ phosphor nanoparticles by Bi³⁺ co-doping". *Optics Express* 32 (23) (2024) 41632-41643 <https://doi.org/10.1364/OE.542685>
3. J. Periša, S. Kuzman, A. Ćirić, Z. Ristić, Ž. Antić, M. D. Dramićanin, B. Milićević. "Tuneable Red and Blue Emission of Bi³⁺-Co-Doped SrF₂:Eu³⁺ Nanophosphors for LEDs in Agricultural Applications". *Nanomaterials* 14(20), 1617. <https://doi.org/10.3390/nano14201617>
4. K. Milenković, V. Đorđević, I. Zeković, Z. Ristić, J. Periša, B. Milićević, M. D. Dramićanin: "Microwave-assisted solvothermal method for RbY₃F₁₀ doped with Eu³⁺"- The 7th International Conference on the Physics of Optical Materials and Devices & The 4th International Conference on Phosphor Thermometry (ICOM&ICPT 2024), August 26-30, 2024, Bečići, Budva Montenegro, P-50, (pp 165).
5. S. Kuzman, B. Milićević, J. Periša, A. Ćirić, Z. Ristić, Ž. Antić, M. D. Dramićanin: "Synthesis and photoluminescent properties of Bi³⁺-codoped SrF₂:Eu³⁺ phosphor nanoparticles"- The 7th International Conference on the Physics of Optical Materials and Devices & The 4th International Conference on Phosphor Thermometry (ICOM&ICPT 2024), August 26-30, 2024, Bečići, Budva Montenegro, P-51, (pp 166).

6. B. Milićević, A. Ćirić, Z. Ristić, M. Medić, I. Radosavljevic Evans, Ž. Antić, M. D. Dramićanin: "Synthesis, luminescent properties, and thermal stability of Eu^{3+} -doped Sr_2GdF_7 red-emitting nanophosphor for horticulture LEDs"- The 7th International Conference on the Physics of Optical Materials and Devices & The 4th International Conference on Phosphor Thermometry (ICOM&ICPT 2024), August 26-30, 2024, Bečići, Budva Montenegro, P-53, (pp 168).
7. K. Milenković, V. Đorđević, S. Kuzman, J. Periša, B. Milićević, Miroslav D. Dramićanin: "Three-fold enhancement of Eu^{3+} emission intensity in BaYF_5 nanoparticles by Bi^{3+} co-doping", -12th International Conference on Luminescent Detectors and Transformers of Ionizing Radiation (LUMDETR), June 16-21, 2024, Riga, Latvia, PA13, (pp 89).
8. S. Kuzman, B. Milićević, K. Milenković, J. Periša, M. D. Dramićanin: "Bismuth-sensitized Eu^{3+} luminescent LED technology for effective indoor plant growth"- The 3rd Serbian Conference on Materials Application and Technology (SCOM2024), October 16-18, Belgrade, Serbia, I-1, (pp 8).
Invited talk

LEDtech-GROW team members reached **Milestone M1.2 - High-performance phosphors selected** (verification: Superior moisture resistance, $\text{QE} > 50\%$, $\text{FWHM} < 50 \text{ nm}$, and low thermal quenching of luminescence up to $150 \text{ }^\circ\text{C}$). The list is as follows:

1. Sr_2GdF_7 :80 mol% Eu^{3+} nanoparticles ($\text{QE}=60.4\%$, Thermal stability= 83%)
2. SrF_2 :10mol% Eu^{3+} , 20mol% Bi^{3+} nanoparticles (highest red/blue emission portion 40.8 : 59.2).
3. BaYF_5 :10mol% Eu^{3+} , 20mol% Bi^{3+} nanoparticles (energy transfer efficiencies (η_T) of 16%).